2012

Finite Element Analysis of a Femur to Deconstruct the Design Paradox of Bone Curvature

Sameer Jade
University of Massachusetts Amherst, sjade@engin.umass.edu

Finite element analysis of a femur to deconstruct the design paradox of bone curvature

A Thesis Presented

by

SAMEER JADE

Submitted to the Graduate School of the
University of Massachusetts Amherst in partial fulfillment
of the requirements for the degree of

MASTER OF SCIENCE IN MECHANICAL ENGINEERING

September 2012
MECHANICAL ENGINEERING

Finite element analysis of a femur to deconstruct the design paradox of bone curvature

A Thesis Presented

by

SAMEER JADE

Approved as to style and content by:

_____

Ian R. Grosse, Chairperson

_____

David S. Strait, Member

_____

Frank C. Sup, Member

_____

Donald L. Fisher, Department head, Department of Mechanical and Industrial Engineering

ACKNOWLEDGEMENTS

First and foremost, I would like to express my sincere gratitude to my advisor, Professor Ian R. Grosse, for his guidance and support during the entire course of my M.S. study at the University of Massachusetts Amherst. His patience, upbeat attitude and knack for offering the correct piece of advice at the correct time were invaluable in keeping me on track to help me reach to this point in my research and without his support this thesis would not have materialized. I am grateful to the committee members, Professor Frank C. Sup and Professor David S. Strait for agreeing to serve on the thesis committee and providing valuable feedback and suggestions.

I would also like to thank all my lab mates for making the lab a fun place to work. It was an absolute pleasure to have met each one of them. A special thanks goes to Lu Huang and Krishna Samavedam for their thoughtful comments and suggestions.

I extend my heartfelt thanks to my friends Dilip Joy, Shiril Tichkule, Shreyas Panse, Ameya Phadke, Sandeep Pillai, Nathaniel DeVelder, Suyash Chaudhary, Ved Chatterjee and Merwyn Cheruvathur for their moral support and advices.

Finally, I would like to thank my parents, family members and friends for their constant support and encouragement during testing times. I would also like to thank the professors who made the courses I took interesting and also a learning experience during my Masters.

ABSTRACT

FINITE ELEMENT ANALYSIS OF A FEMUR TO DECONSTRUCT THE DESIGN PARADOX OF BONE CURVATURE

SEPTEMBER 2012

SAMEER JADE

B.S.M.E, UNIVERSITY OF PUNE, INDIA

M.S.M.E, UNIVERSITY OF MASSACHUSETTS AMHERST

Directed by: Professor Ian R. Grosse

The femur is the longest limb bone found in humans. Almost all the long limb bones found in terrestrial mammals, including the femur studied herein, have been observed to be loaded in bending and are curved longitudinally. The curvature in these long bones increases the bending stress developed in the bone, potentially reducing the bone's load carrying capacity, i.e. its mechanical strength. Therefore, bone curvature poses a paradox in terms of the mechanical function of long limb bones. The aim of this study is to investigate and explain the role of longitudinal bone curvature in the design of long bones. In particular, it has been hypothesized that curvature of long bones results in a trade-off between the bone's mechanical strength and its bending predictability. This thesis employs finite element analysis of human femora to address this issue. Simplified human femora with different curvatures were modeled and analyzed using ANSYS Workbench finite element analysis software. The results obtained are compared between different curvatures including a straight bone. We examined how the bone curvature affects the bending predictability and load carrying capacity of bones. Results were post processed to yield

probability density functions (PDFs) for circumferential location of maximum equivalent stress for various bone curvatures to assess the bending predictability of bones. To validate our findings on the geometrically simplified ANSYS Workbench femur models, a digitally reconstructed femur model from a CT scan of a real human femur was employed. For this model we performed finite element analysis in the FEA tool, Strand7, executing multiple simulations for different load cases. The results from the CT scanned femur model and those from the CAD femur model were then compared. We found general agreement in trends but some quantitative differences most likely due to the geometric differences between the digitally reconstructed femur model and the simplified CAD models. As postulated by others, our results support the hypothesis that the bone curvature is a tradeoff between the bone strength and its bending predictability. Bone curvature increases bending predictability at the expense of load carrying capacity.

TABLE OF CONTENTS

Page

LIST OF TABLES

Table Page

LIST OF FIGURES

CHAPTER 1

INTRODUCTION

1.1 Introduction

This study is focused on the femora of mammals. The femur is the longest and the largest bone found in the human body. The femur is also called the thigh bone. It connects to the pelvis at the proximal end to form the hip joint and to the tibia at the distal end to form the knee joint. The femur in the body takes the largest percentage of the weight of the body. The shaft of the femur is cylindrical with approximately circular cross section shape and is found to possess a longitudinal bon eccentricity or shape eccentricity [1-3], as can be seen in Fig. 1 and Fig. 4.

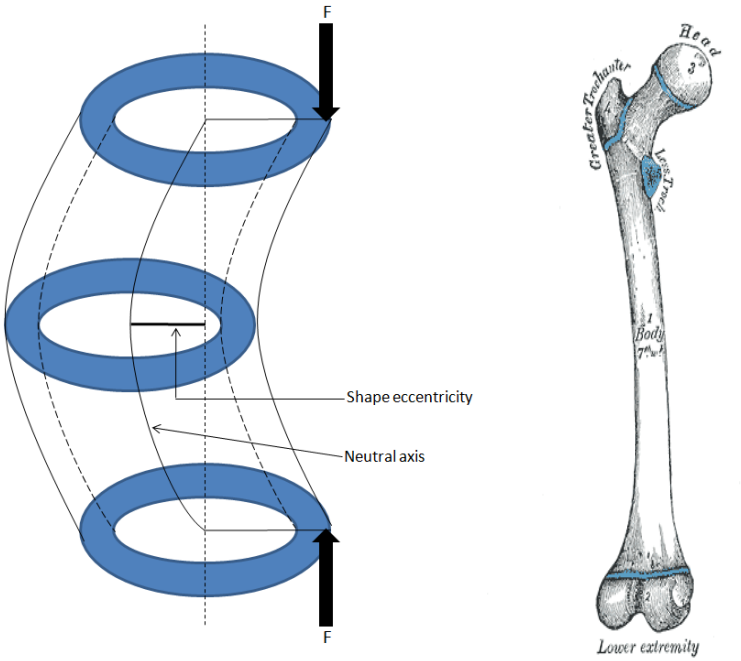

Figure 1. A human femur [4]

It is important to note here that various authors [3, 5, 6] in the past have used the term bone curvature to define what we call bone eccentricity in this study. Curvature is mathematically defined as the reciprocal of the radius of curvature. Therefore, in this study we

redefine what others have called bone curvature [3, 5, 6] as bone eccentricity in order to be mathematically more accurate. The mathematical relationship between a true bone curvature, c and its radius of curvature, R_c with the shape eccentricity, e_s is as follows.

$$R_c = \frac{1}{c} = \frac{4e_s^{\,2} + L^2}{8e_s} \tag{1}$$

where, L is the length of the bone. By dimensionalizing equation (1) using L, equation (1) can be re-written as,

$$\frac{R_c}{L} = \frac{1}{cL} = \frac{4(\frac{e_s}{L})^2 + 1}{8(\frac{e_s}{L})} \tag{2}$$

To better understand the relationship between the radius of curvature of bone, true bone curvature and its shape eccentricity, we plotted the radius of curvature of bone and bone's true curvature against the shape eccentricity of the bone using equation (2).

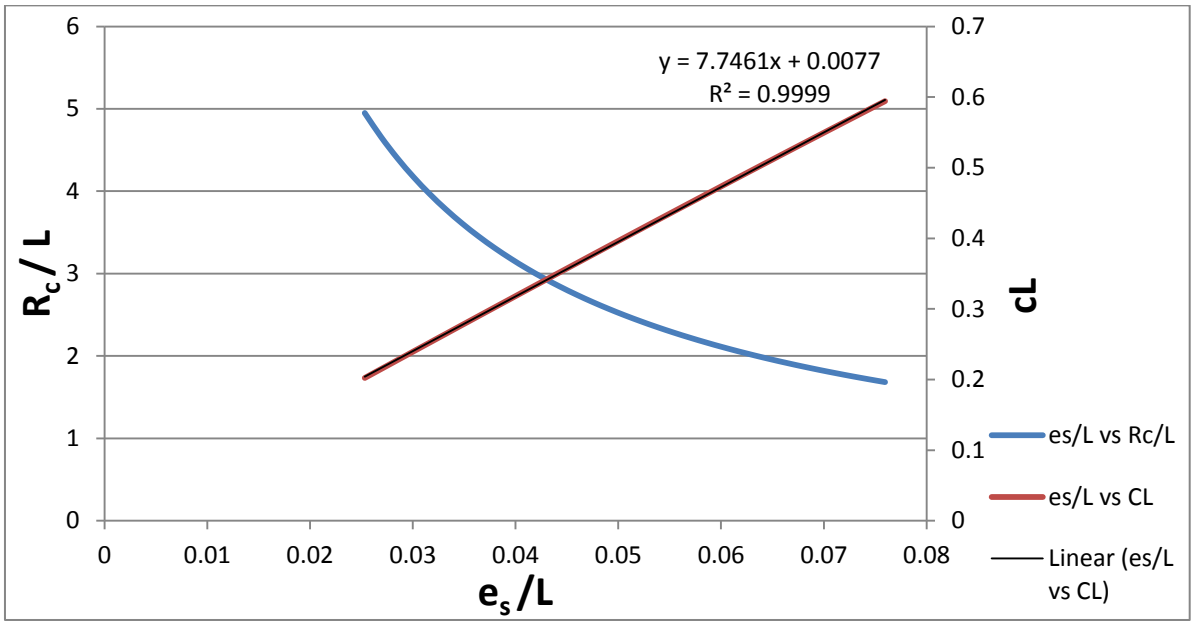

Figure 2.R_c/L and cL plotted against e_s/L.

The curve of $\frac{R_c}{L}$ vs. $\frac{e_s}{L}$ shows that the radius of curvature of the bone is inversely proportional to the shape eccentricity of the bone. And the curve of cL vs. $\frac{e_s}{L}$ shows that the true bone curvature increases monotonically with the shape eccentricity. Also, for the range of shape eccentricity considered, the relationship between shape eccentricity and true bone curvature is nearly perfectly linear.

The bones' shape eccentricity is defined as the perpendicular distance taken from the center of the line joining the centers of the bone cross sections at the proximal and distal ends to the point mid way on the neutral axis of the bone. This shape eccentricity makes the axial force acting on the bone produce a bending moment about the mid-shaft [3].

There are two main parts involved in this study; firstly, to find how the bone curvature affects the bone's mechanical strength, and secondly to find how the bone curvature affects it's bending predictability. A bone's mechanical strength is defined as the largest load that can be supported elastically by the bone. Bending predictability is defined as the probability of the bone to bend in a certain direction or the predictability of pattern of stresses in a bone.

1.2Background

One of the earliest discussions on the mechanical significance of curvature of long bones of mammals was carried out by John Bertram and Andrew Biewener in their research paper, "Bone curvature: sacrificing strength for load predictability" [5]. The authors here questioned the role of bone curvature in the design of the long bones of mammals. The authors noted that a straight bone should be most efficient in design because of the maximum mechanical strength of a straight bone. For a given load bending generates much higher stresses in the bones than pure

axial compression, since in bending the external surface is subjected to high stresses [5]. As a result, the bones that are subjected to bending have lower mechanical strengths than the bones subjected to pure axial compression. In spite of this, the long limb bones in mammals have been found to be predominantly loaded in bending [1, 7]. Mechanical strength here refers to the bones' load carrying capacity which is its ability to withstand loads elastically. Material strength means the bones' ability to resist permanent deformation and cracking. Material strength is a part of mechanical strength. It has also been studied that in the limb bones of mammals, the largest proportion of total strain and total stress is due to the bending moment rather than the axial force [1]. Hence there is a paradox in the design of the bone. The bending moment in the bones is produced by the eccentric loading due to the dynamic loading environment that the bone is subjected to and secondly because of the longitudinal curvature present in the bone [3]. A dynamic loading environment refers to the loads that act on long bones resulting from motions including walking, running, jumping, climbing stairs etc. Biewener had theorized that in case of tibia and ulna bones the bone curvature causes an increase in the overall stress in the bone. However, Biewener also said that the curvature present in femur attempts to reduce the total bending that the bone is subjected to by counteracting the bending moment produced by the eccentric axial forces [8]. This was supported by Frost, who hypothesized that the curvatures in long bones are present mostly to decrease the overall bending stress in the bones [9]. Nonetheless, many studies have suggested that the longitudinal bone curvature increases the total bending stress developed in the bones [1, 3, 7]. One of the possibilities in this could be that the relation between the long limb bone shapes and their overall bending or mechanics is somewhat different for different bones [10].

It has been postulated by Lanyon that the longitudinal bone curvature in long bones may be present to generate a certain minimum level of strain in the bone, essential for healthy functioning of bones or for the convenience of good packing of the surrounding muscles [8]. However these hypotheses were not backed with sufficient data[10].

A lot of attention has been given to the effect of longitudinal bone curvature present in the mammal limb bones to the bone strength and the contribution of bending to the total stress generated [1, 6, 7]. However, not much research has been done to understand how the longitudinal bone curvature affects the bending predictability of the bones. Bending predictability is defined as the probability of the bone to bend in a certain direction or the predictability of pattern of stresses in a bone.

For structures like long limb bones of mammals that are exposed to variable dynamic loads and unpredictable loading environment, it is very improbable to be subjected to pure axial loads. This is because the off-axis loading on the bone and the bone curvature causes some bending in the bone[5]. Therefore, the bone curvature assists the bone to be loaded in bending. This feature in the long limb bones subjected to loads in variable directions could give mammals a mechanical advantage of improved bending predictability which restricts the range of bending direction of the bones. On the other hand, a straight bone subjected to loads in variable directions will have no restriction on the range of its bending direction and hence will have no bending predictability [5]. A possible advantage of bending predictability is that it enables the mammals to increase their bone's material strength non-uniformly based on where the maximum probability of maximum stress occurs. However, we have no evidence to support this at this point.

1.3Past Analytical Work

The paradox of the bone curvature was initially researched by Bertram & Biewener when they introduced the concepts, 'bending predictability' and 'load carrying capacity' to be important design features of long limb bones. Therefore, the effects of both these features on the design of bones were studied to check whether there existed a tradeoff between these two design features.

The load carrying capacity of a structure is the ability of the structure to elastically support a load. For curved bones Bertram & Biewener defined its load carrying capacity in a relative context- the maximum load that can be supported elastically by a curved bone relative to the maximum load that can be supported by a straight bone of the same material strength. Further, they assumed the load to be applied in the axial direction at a point which is in the plane of curvature of the bone. An expression of load carrying capacity in terms of radius of bone cross section and the curvature of bone was derived. Another assumption made by the authors in their derivation of [5] is that the bone has a circular, solid cross section. Fig 5 shows the geometry of the bone used for the derivation.

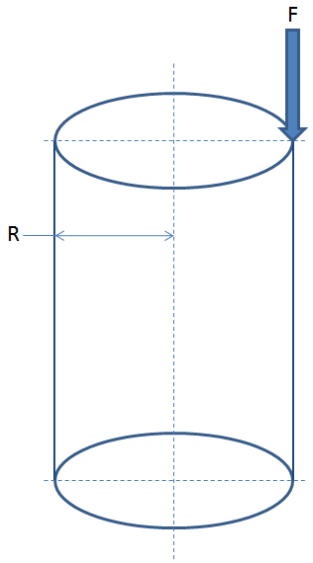

Figure 3. A straight bone

Assuming F to be the maximum load supported by a straight bone, the total "normal" stress generated in the bone is given by the normal stress due to force acting normal to the section plus the normal stress due to bending:

$$\sigma_{max} = \frac{F}{A} + \frac{M(c)}{I} \tag{3}$$

where M is the bending moment given by FR, R is the radius of bone cross section, c is the perpendicular distance to the neutral axis from outermost fiber of the column, A is the cross sectional area given by πR^2 for a circle and I is the second moment of inertia given by $\pi R^4/4$ for a circle.

Note that Eq.(3) assumes that the normal stress due to axial load and the normal stress due to bending are of the same sign, and the sense of maximum stress as compression or tension is not accounted for in Eq. (3). Thus, for an axial load that results in compression, then the compressive bending stress is added to the axial normal stress to obtain the maximum normal stress. Using the appropriate relationships for the terms shown in Eq. (3) for a solid round section, one gets:

$$\sigma_{max} = \frac{F}{\pi R^2} + \frac{F(R)(R)}{(\frac{\pi}{4}R^4)} \tag{4}$$

Now a bone which is curved longitudinally is considered. Let f be the load acting in line with the curvature of the bone as shown in Fig 4. Fig 4 shows the side view of a symmetrical half bone. The total stress produced by load 'f' on the curved bone is calculated.

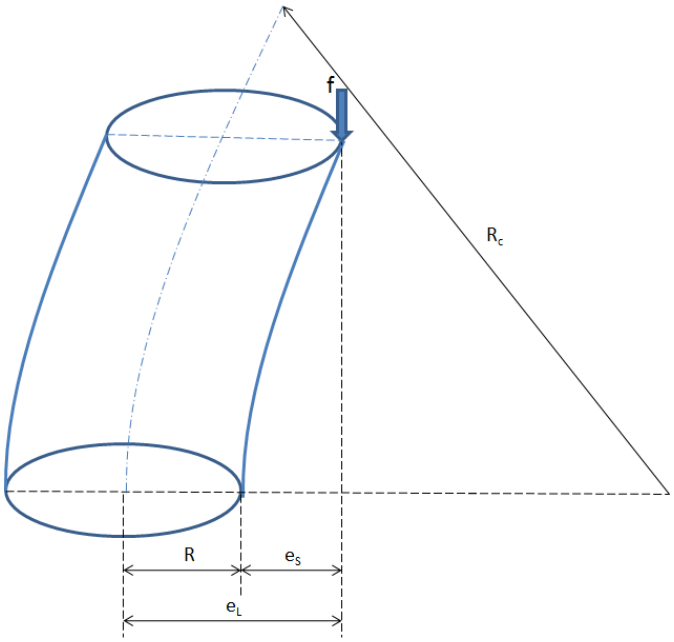

Figure 4. A curved bone with symmetrical half length showing shape and load eccentricity

The total stress is given by Equation (3) again but now the bending moment M is given by fe_L, e_L is the load eccentricity given by $R+e_S$ and e_S is the shape eccentricity as shown in Fig 4. All other parameters are same as before. Therefore, we get:

$$\sigma_{max} = \frac{f}{\pi R^2} + \frac{f(R+e_s)(R)}{(\frac{\pi}{4}R^4)} \tag{5}$$

Note that our notation and terminology are different than that presented by Bertram & Biewener. Bertram & Biewener used the term bone curvature (c) to refer to what we designate here as shape eccentricity. In analytical geometry, curvature (c) is mathematically defined as the inverse of the radius of curvature (R_c). Further Bertram & Biewener do not define the load eccentricity, which is important for determining the bending moment induced by the axial load.

Now, by equating the two expressions of total stresses, we get the 'relative load carrying capacity', RLCC which is given by 'f/F' in terms of curvature.

$$RLCC = \frac{f}{F} = \frac{(5)}{(5) + 4(\frac{e_s}{R})} \tag{6}$$

Next, we derived an expression for relative load carrying capacity (RLCC) of a hollow bone to compare its results with those of the solid bone. Following the same procedure but with a hollow cross section, we obtain an expression for load carrying capacity, RLCC as:

$$RLCC = \frac{f}{F} = \frac{(5R_1^{\,2} + R_2^{\,2})}{(5R_1^{\,2} + R_2^{\,2} + 4R_1 e_s)} \tag{7}$$

where R_1 is the outer radius and R_2 is the inner radius of the bone cross section. The mean dimensions of $R_1$and cortical bone thickness were obtained from [11] and [12].

The authors in [11] obtained femoral measurements from 72 intact human adult femora of a contemporary Central Anatolian population. The femora were obtained from the teaching skeletal collections at the Anatomy Department of the Medical School, University of Selçuk. This gave R_1 = 13.375 mm and R_2 = 6.325 mm [11].

Various values of RLCC were calculated for different h/R values and then RLCC was plotted against e_S / R (see Figure 5).

Table 1. Values of RLCC formulated for different normalized eccentricity values

Bone eccentricity, e_S /R	**Relative Load carrying capacity, RLCC**	
	Solid bone	**Hollow bone**
0	1	1
0.6	0.6756757	0.685189412
0.9	0.5813953	0.592004732
1.2	0.5102041	0.52113165
1.5	0.4545455	0.46541368
1.8	0.4098361	0.42045932
2.1	0.3731343	0.383424321
2.4	0.3424658	0.352385424
2.7	0.3164557	0.325995494

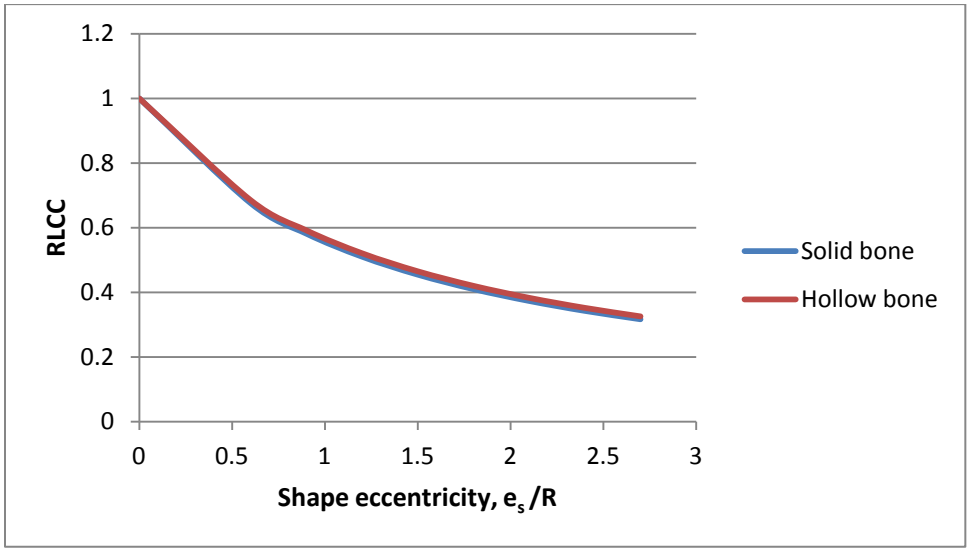

Figure 5. RLCC plotted against e_s/R [5]

It can be seen from Fig. 5 that the relative load carrying capacity is maximum at zero curvature i.e. for a straight column, and it reduces monotonically with increasing shape eccentricity. Hence shape eccentricity reduces the relative load carrying capacity of the bone. Also, we can observe no substantial difference for the RLCC between solid and hollow bones. Bertram & Biewener in their study have the point load applied all around the circumference with the position of load defined by angle α as shown in Fig. 6, and the location of maximum bending stress is defined by angle ϕ.

Now, for evaluating bending predictability, firstly the angles 'α' and 'ϕ' have to be defined. Alpha (α) was defined as the location of the external point load acting on the bone's circumference measured from the plane of curvature as shown in Fig 6. Phi (ϕ) denotes the location of the maximum stress on the bone. ϕ is measured from the plane of curvature to the line joining the point of load application to the center of midsection as shown in Fig. 6. ϕ is

measured at midsection because bending will cause maximum stresses at the midsection of the bone.

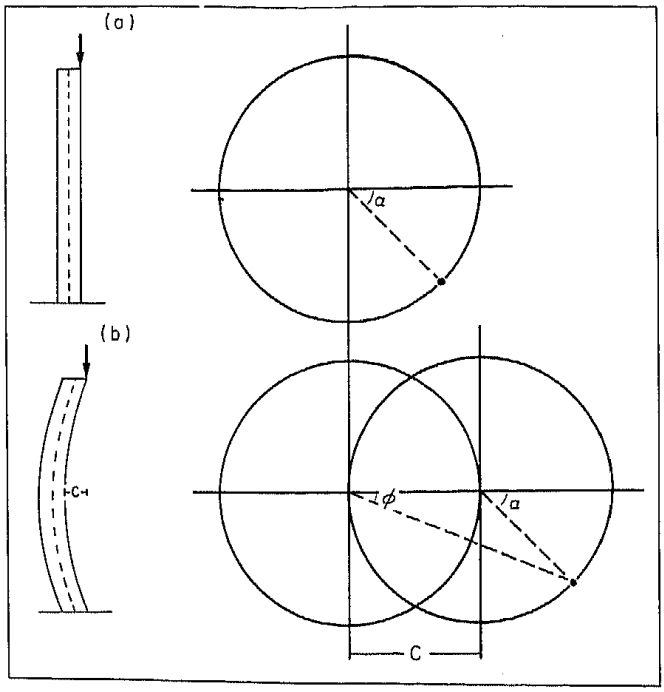

Figure 6. Peripheral point load model showing a) A straight bone with a point load acting at an angle α. b) A curved bone with a longitudinal bone eccentricity denoted as 'c' and load acting at an angle α and direction of bending denoted by angle Φ. In fig (b), the circle on the right corresponds to the top section of the bone and the circle on the left corresponds to the mid section of the bone. [5]

In Fig 6 given by [5], the shape eccentricity is denoted as 'C'. However, in this study we denote shape eccentricity as e_S, as shown in Fig 3. ϕ is evaluated by applying basic trigonometry, and is given by the relation:

$$\phi = \tan^{-1} \frac{(R\sin\alpha)}{(R\cos\alpha + e_s)} \tag{8}$$

Note: The expression for ϕ was incorrect in Bertram & Bieweners' paper [5]. Therefore the following graphs are evaluated from the corrected expression and therefore are different from those in the referred paper.

The expression of ϕ for a hollow bone remains the same as that for a solid bone as shown in Eq. (8). Therefore the bending predictability computed in the following section is same for a solid and a hollow bone. Using the relation, ϕ was calculated for various α values ranging from 0-180 degrees and for various shape eccentricity (e_S) values and plotted (see Fig. 7).

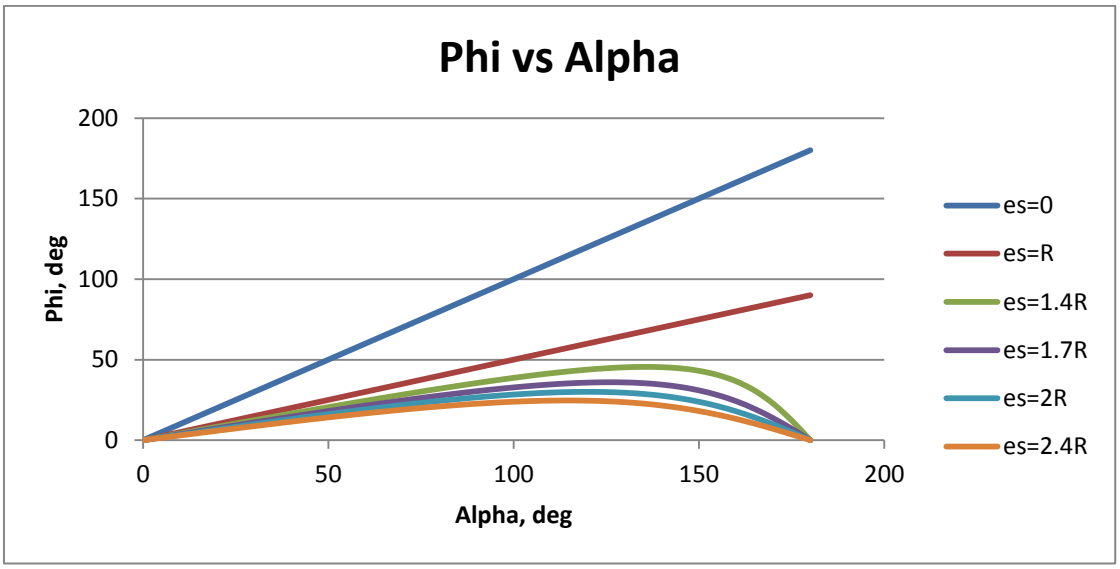

Figure 7. Phi vs. Alpha (For solid and hollow cross section)

It can be observed from the graph above that as the shape eccentricity raises, the range of ϕ decreases. Also, we note that for a straight bone (e_S =0), the range of ϕ is equal to the range of α. Bertram & Biewener introduced the term relative variability (V_r) in order to normalize the range of ϕ as given by:

$$V_r = \frac{range\ \phi}{range\ \alpha} \tag{9}$$

where range ϕ = maximum ϕ – minimum ϕ and range α = maximum α – minimum α.

As the shape eccentricity increases, the range of ϕ reduces and therefore the relative variability(V_r) reduces. As the relative variability decreases, the bending predictability (P_b)also increases. The authors defined bending predictability as given by:

$$P_b = 1 - V_r \tag{10}$$

Bending predictability (P_b) can be loosely interpreted as the probability of the bone to bend in a certain direction or the predictability of pattern of stresses in a bone [5]. Bending predictability(P_b)is plotted against e_S normalized with R to analyze the behavior of bending predictability with change in shape eccentricity.

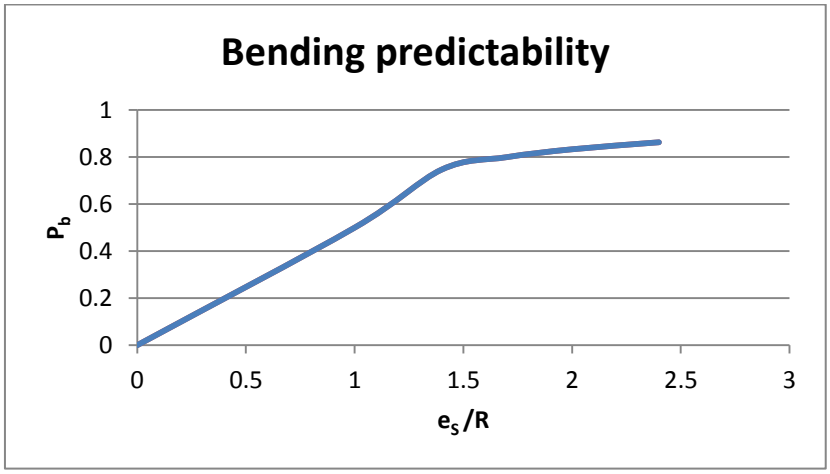

Figure 8. Bending predictability vs. shape eccentricity (For solid and hollow cross section)

It can be observed from Fig. 8 that the bending predictability of the bone increases with increase in shape eccentricity. With both the results of load carrying capacity and bending predictability, it was concluded that the shape eccentricity was a trade-off between bone strength and bending predictability. Although these results give us an idea of how the shape eccentricity of the bone affects the bone strength and bending predictability, we find some areas which may need better analysis. While evaluating the load carrying capacity, the authors assumed the load to

be only acting in line with the curvature of the bone i.e. for α=0 deg and therefore did not consider different locations of the load while evaluating RLCC.

Also, the bending predictability is evaluated based on the ranges of angle ϕ and is a loose interpretation of the probability density function that reflects the longitudinal plane of bending. Therefore, it may not be a mathematically accurate picture of the probability density function for the angle ϕ for different shape eccentricities, separately. Bertram & Biewener's bending predictability does not tell us on which longitudinal plane the bone is most likely to bend for a particular shape eccentricity and range of α values and how that location changes for different shape eccentricities. A more informative representation would be realized by developing probability density function graphs for various e_S values depicting the frequency of occurrence of ϕ for each e_S value.

Moreover, all the results have been obtained analytically using analytical mechanics applicable for simple geometry. In order to validate the results obtained by [5]in the context of more realistic bone structures, we employed finite element analysis, FEA in the following chapter to revisit the study of Bertram and Biewener.

1.4 FEA in Physical Anthropology and Comparative Biology

Finite element method (FEM), also called finite element analysis (FEA) is a part of computer-aided engineering (CAE) which is basically employing computer software's for solving engineering tasks. FEA is a numerical method which is used for evaluating stress, strain and deformation of complex structures. It does that by converting a complex geometry into a mesh of finite elements with simpler geometries which are connected to each other by nodes. Then, the real life conditions on the structure are simulated upon the 3 D model by applying appropriate boundary conditions, loading conditions and material properties. The accuracy of the solution

can be increased by making the mesh finer; although, even with a very fine mesh, there remains a slight approximation in the solution. FEA overcomes the limitations of the theoretical and experimental methods using strain gauges, load test machines, mechanical simulators etc[13-15, 15-19].

Finite element modeling and analysis is a technologically advanced method which is becoming widely used in anthropology and comparative biology to study the relationship between form and mechanical function of biological structures [20, 21]. A substantial amount of research been done in this field of applying FEA to physical anthropology and comparative biology [22-42]. FEA has been used in a very wide area of biology ranging from performing analysis in exoskeletons, orbital mechanics, hip joints, cardiovascular biomechanics, skulls, bones, biting force of teeth and ligaments to name a few [21, 26, 29, 30, 42-48]. In cases where the experimental or in vivo measurements are not possible or inaccurate, FEA has helped in analyzing and answering questions in functional morphology for example- predicting bite forces in mammals, material behavior of bones and teeth in mammals etc [24, 30]. FEA therefore helps in creating a link between biology and mechanics. FEA is used often in the field of biology for addressing questions regarding the form-function relationships, morphology and evolution of various organisms[20]. Finite element analysis method overcomes the limitations of theoretical and experimental approaches by reducing complex geometries into a mesh of finite elements with simpler geometries. The experimental and theoretical methods using strain gauges, load test machines, mechanical simulators etc work well with simple structures but they have their limitations when the structure is complex which is usually true for biological structures like bones[13, 20, 49]. Also the dynamic loading that the biological structures are subjected to, adds

up to the complexity of their analysis. Therefore, finite element analysis has become a very popular method for carrying out different studies in evolutionary biomechanics.

In this study, we employ FEA method to study the form function relationship in a femur. Form function relationship is based on the principle of form follows function which says that the shape of an object or a structure should essentially be based upon its intended function or requirement[50].

CHAPTER 2

MATERIALS AND METHODS

2.1Finite element modeling & analysis

2.1.1 Finite element modeling

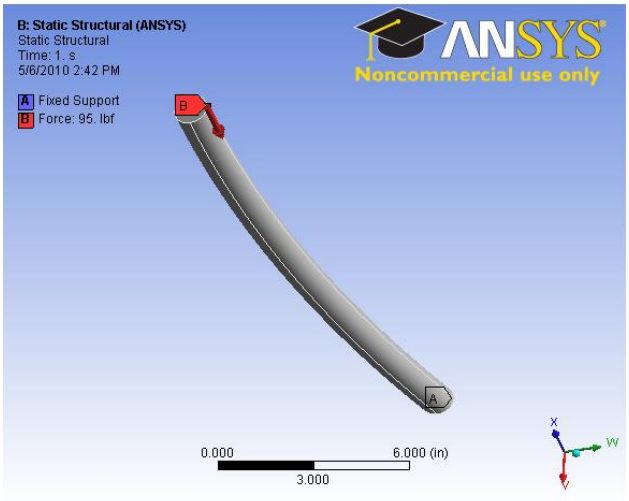

Figure 9. Initial bone model

We used ANSYS® Workbench™ v 13.1[1] for the 3D modeling and analysis of the femur. We modeled the human femur as a curved hollow cylinder with circular cross section in ANSYS Workbench Design Modeler. The bone was modeled with the bone axis along the Z axis. The radius of curvature of the bone and the location of the load were parameterized since we wanted to study the behavior of bone for different locations of the load and for different values of bone eccentricities. For the initial model, the entire bone length was modeled with one end fixed supported while on the other end, a peripheral point load was applied as shown in Fig. 9. The point load was applied on the circumference of the bone to account for the misalignment

[1]ANSYS Workbench® is a product of ANSYS, Inc., Canonsburg, PA.

between the load and the bone neutral axis. The average human male weight is around 86 kilograms. Therefore, assuming that half of this load acts on a femur, a load of nearly 450 N was applied on the model. The location of the load is a random variable and therefore can act at any point along its circumference. To address that, the point of application of force was marked using the 'split at select' command in ANSYS Design Modeler which made the point of application of load controllable and the location of load was parameterized from 0 to 180 degrees. But since the bone is symmetric along its length or z axis, modeling only a symmetrical half of the bone along the length with appropriate symmetric boundary conditions will give the same effect as with the full length bone. This reduced the number of elements of the model and thus increased the computational speed. Hence, a new bone was modeled with only half the length as shown in Fig. 10. The different stages of bone modeling are shown in Fig. 10.

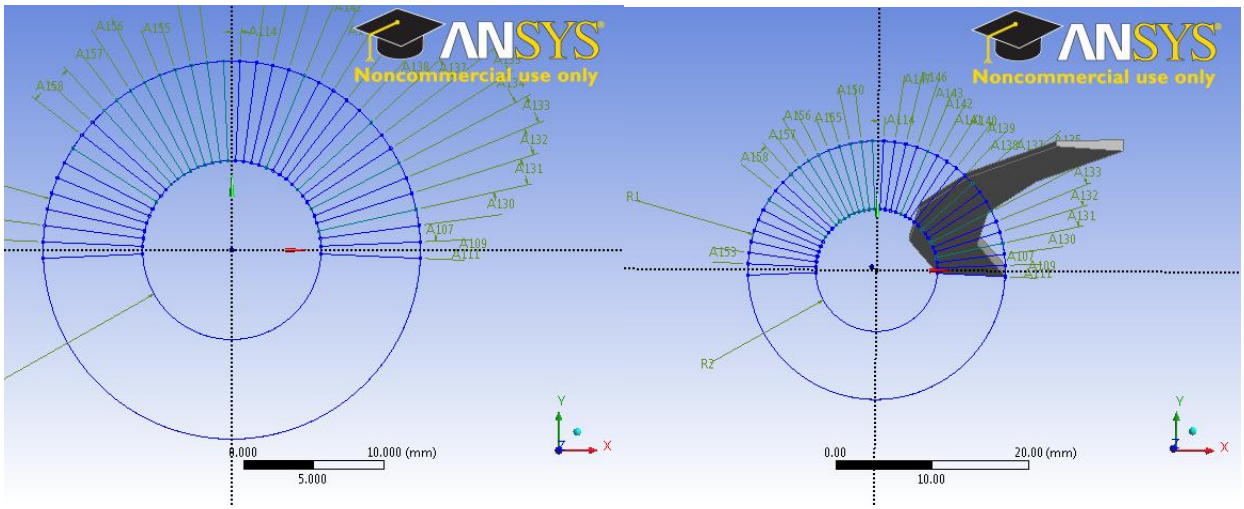

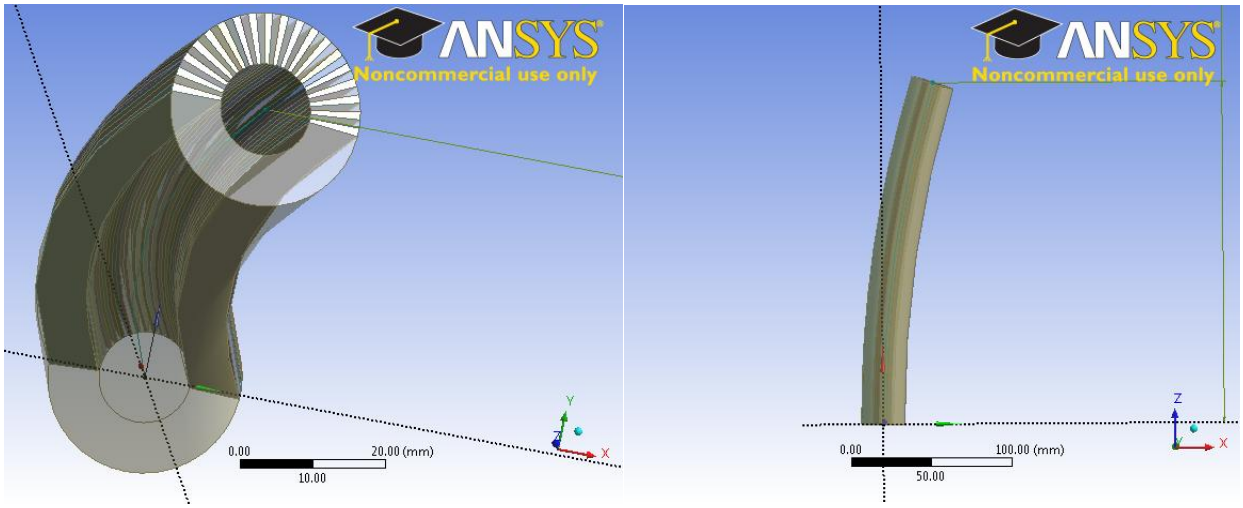

Figure 10. Different stages of bone modeling

In this model, one symmetrical half of the bone about the x axis was divided in 36 equal sections of 5 degrees each as shown in Fig.10. This was done to enable application of a surface load on any of those 36 patches independently and therefore the location of the load was parameterized between 0 – 180 degrees as shown in Fig 11 in discrete 5 degree increments. The patches were made using the 'Add material' and 'Add frozen' options alternately available in the sweep operations in the ANSYS Workbench Design Modeler. The radius of curvature was also parameterized in order to perform simulations for different bone eccentricities.

Dimensions used for the finite element model were obtained from [11, 12, 51]. For the bone cross section radius and length [11], the authors obtained femoral measurements from 72 intact human adult femora of a contemporary Central Anatolian population. For the cortical thickness value [12], the authors obtained the data of adult human specimens between 20 and 79 years. And, for the radii of curvature of the bone [51], the authors obtained the radii of curvature from 14 human femora.

Table 2. Bone dimensions used for modeling[11, 12, 51]

Dimension	Value, mm
Bone cross section radius	13.375
Cortical thickness	7.05
Maximum length	422.5
Radii of curvature	689-1885

Then we imported the model into the ANSYS Workbench Mechanical module to perform finite element analysis. Here, we applied boundary and loading conditions to the bone before performing simulations. To account for the symmetry, symmetric boundary conditions were applied in the form of three displacement points on the top and the bottom sections in order to constrain their displacement.

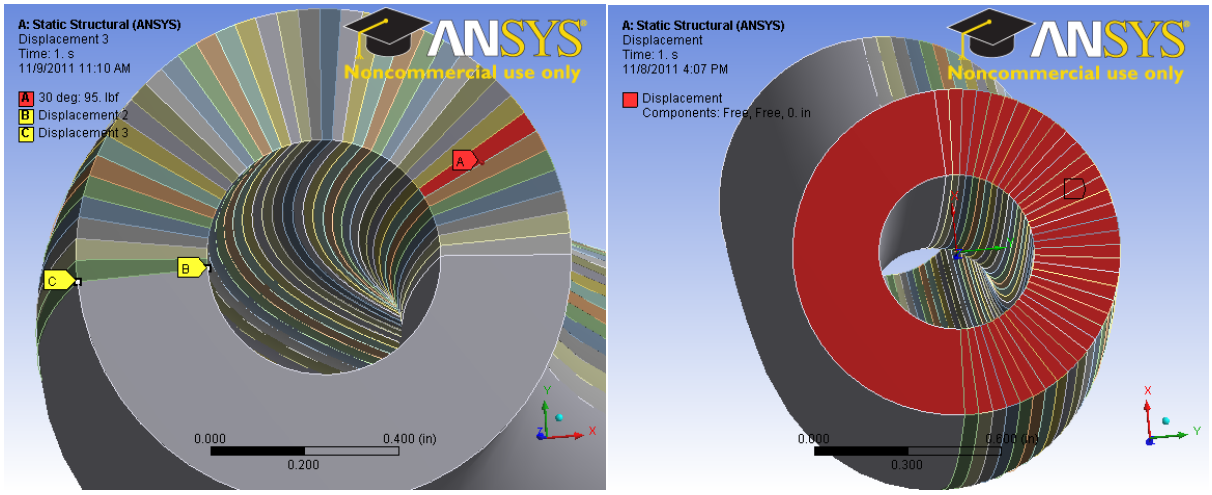

Top face **Bottom face**

Figure 11. The figure on left side shows the bones' top face with 2 displacement points and load applied and the figure on right side shows the bottom face with displacement applied on the face

One displacement was applied on the entire bottom face which is the mid section of the actual bone as shown in Fig. 11 in order to constrain its displacement along z direction. The other

two displacement points were applied on two points on the top face of the bone shown in Fig. 11. These were to constrain the sliding of the bone in x and y directions.

2.1.2 Material properties

The mechanical properties of bones vary according to age, species, anatomical site etc. The outer hard and dense part of the bone is called the cortical bone. Elastic isotropic cortical bone values were used in this study from [52]. Table 3 shows the values of material properties used.

Table 3. Material properties[52]

Property	Value
Young's modulus E (MPa)	17000
Poisson's ration ν	0.33

where E is the Young's modulus and ν is the Poisson's ratio.

2.1.3 CT Scanned femur model

After performing the analysis with remote forces on the femur CAD model, we compared those results in order to validate them. Therefore, as the last part of this study, we performed a study on a CT scanned model[2] of a real human femur and compared the results with the results from the previous section. The model was imported as a NASTRAN file and it was then saved in Strand7 software[3] as a st7 file. The model has 238,775 nodes and 1,271,957 4-noded tetrahedral bricks. This femur model consisted of a cortical shell along the bones' diaphysis and two trabeculae or cancellous parts in the proximal and the distal ends (epiphysis). The material properties of this model are as follows,

[2] The CT Scanned model of human femur was built and provided by Kelli Tamvada, doctoral candidate at the Department of Anthropology, University of Albany, NY and Professor David S. Strait, Associate professor of Anthropology, University of Albany (SUNY), NY.

[3] Strand7® is a product of Strand7 Pty Ltd, University of Sydney and the University of New South Wales, Australia.

Table 4. Material properties

	Cortical	Cancellous
Young's modulus E (MPa)	20,000	749
Poisson's ration ν	0.3	0.3

Load analysis similar to the previous chapter was performed here. The orientation of the load is explained in Fig. 12 and Fig. 13 with angles β and γ defined. Angle β ranged from 0 to 30 degrees with increment of 2 degrees.

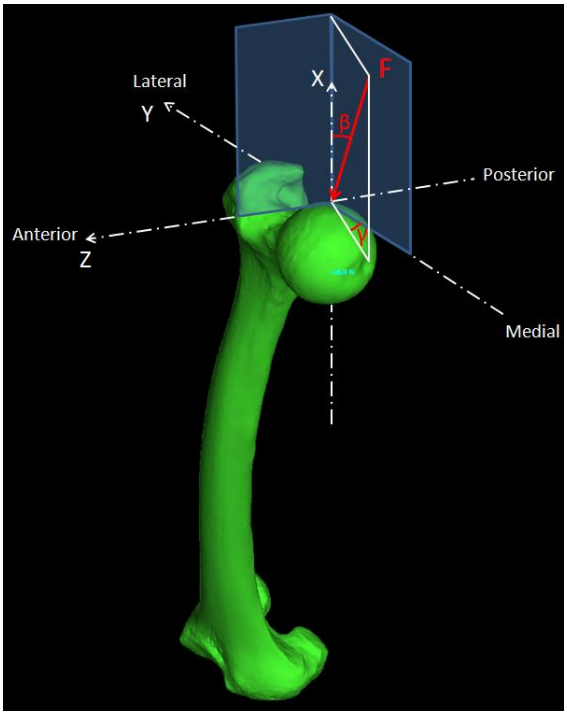

Figure 12. 3D view of the CT scanned femur model showing force orientation with angles Beta and Gamma defined as shown.

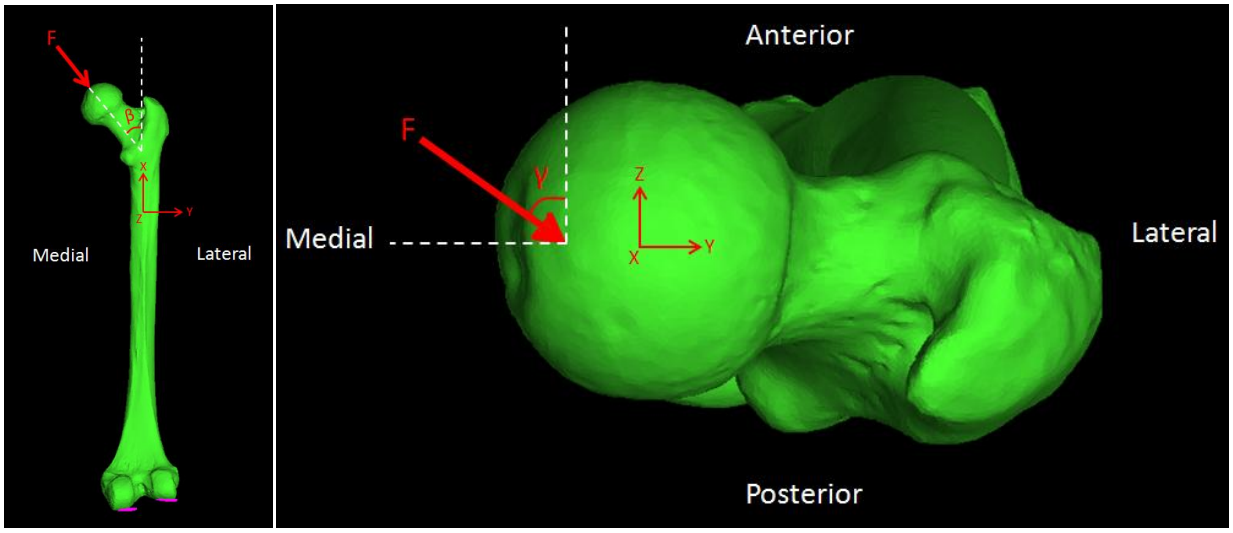

Figure 13. 2D anterior and top views of the CT scanned femur model in Strand7 with angles Beta and Gamma indicated.

For boundary conditions, displacement points were applied on the bottom face of the bone with displacement in x, y and z directions constrained as shown in Fig. 14.

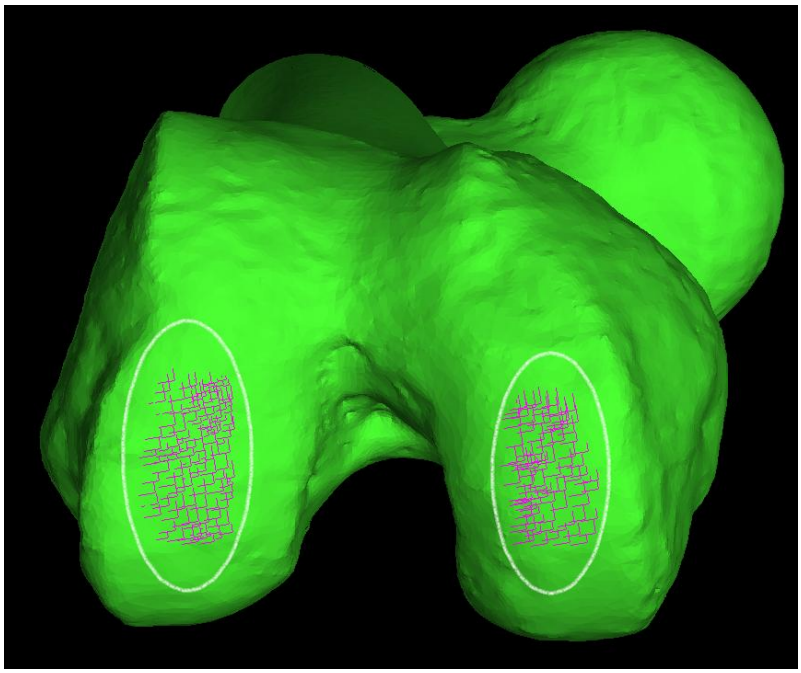

Figure 14. Displacement points applied on the bottom face of the bone. The displacement points applied are circled above.

We then evaluated the critical dimensions of the CT Scanned femur model. For evaluating the radius of curvature, we used the normalized curvature moment arm (NCMA) or the included angle method [53, 54].

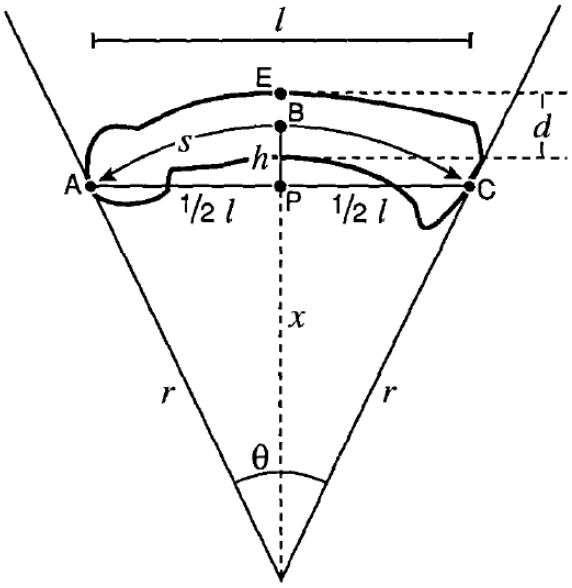

Figure 15. Landmarks and distances indicated in a phalanx (finger bone) for measuring the curvature [53]**.**

In this method, the curve of the bone is assumed to be a part of the circumference of a circle as shown in Fig. 15. Based on the included angle Θ and applying geometric relations, radius of curvature was evaluated.

2.2Analytical analysis

For the analytical analysis part, we re-evaluated the analytical results based on our CAD femur model's geometry and loading conditions. The results obtained were compared with the results that we obtained from finite element analysis of the CAD femur model. In our analytical model we assumed the bone to be hollow and the load to be acting on surface patches similar to the CAD model. Since we apply the load on surface patches, the load effectively acts as a point load on the centroid of the surface patch as shown in Fig. 16.

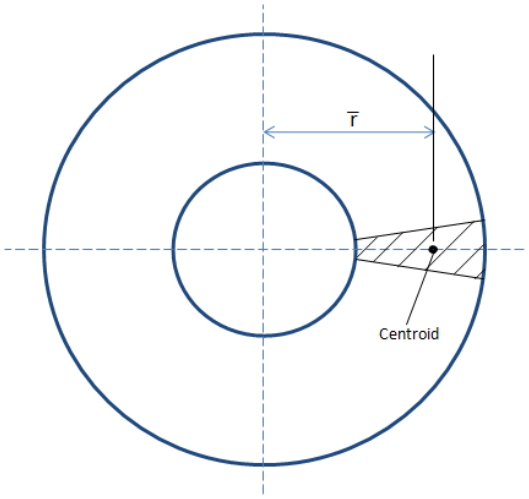

Figure 16. Top face of the bone showing the dimension, $\bar{r}$

Fig. 17 shows the top view of the top section and the mid-section of the bone.

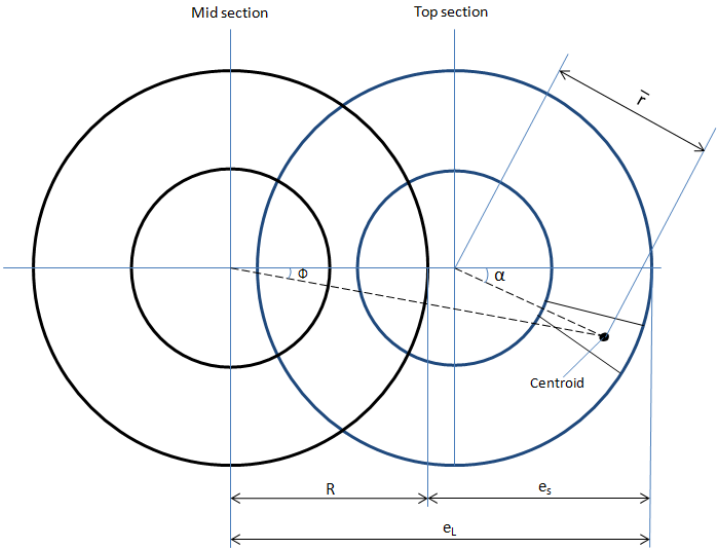

Figure 17. Top view of the top section and the mid section of the bone

where '$\bar{r}$' is the distance from the centroid of the surface patch to the center of the cross section as shown in Fig. 17.Using this model, bending predictability and relative load carrying capacity were calculated.

CHAPTER 3

FEA ANALYSIS OF A CAD FEMUR MODEL

3.1 Direct load analysis using the CAD femur model

In this section, we analyzed the CAD model that we built in ANSYS Workbench shown in chapter 2. We performed simulations to calculate the bending predictability, relative load carrying capacity and probability density functions in order to compare our results with the results obtained analytically by Bertram and Biewener and also with the analytical results that we calculate in the further sections.

3.1.1 Bending predictability by FEA results

After modeling the femora, we ran various simulations for locations (α) of the load on all the 36 patches ranging from 0-180 degrees as shown in Fig 11. This was repeated for all five shape curvature (e_s) values of the bone and also for a straight bone. A total of over 200 simulations were run with each simulation providing the magnitude and location (ϕ) of maximum von Mises stress. The value of ϕ was measured from the plane of curvature of the bone as shown in Fig 18. In this study, we calculated all ϕ values manually. However, later we also developed an APDL code which can be used to automatically calculate ϕ and also parameterize ϕ to include it in the table of design points in ANSYS workbench. The APDL code to calculate ϕ is given in APPENDIX E.

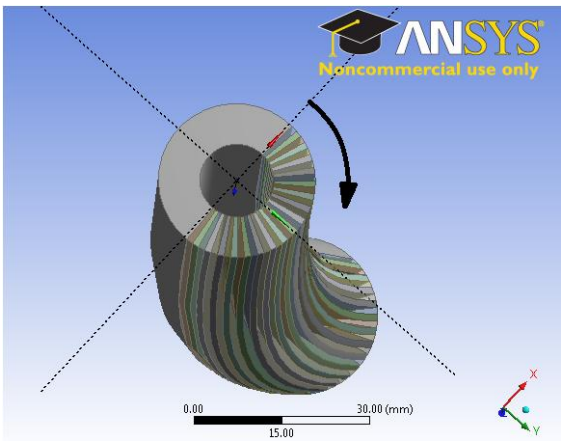

Figure 18. Orientation of Φ

We thus got a set of $\phi_i(\alpha_i)$ values for each shape eccentricity value. The various sets of $\phi_i(\alpha_i)$ values are plotted as points as shown in Fig 20. Fourth degree polynomial curves were then fitted to each set of ϕ_i versus α_i values as shown in Fig 19. Here, i=1,2…..36 for the 36 sections of the bone face where the load is applied. The polynomial equations along with their R^2 values are provided in

APPENDIX .

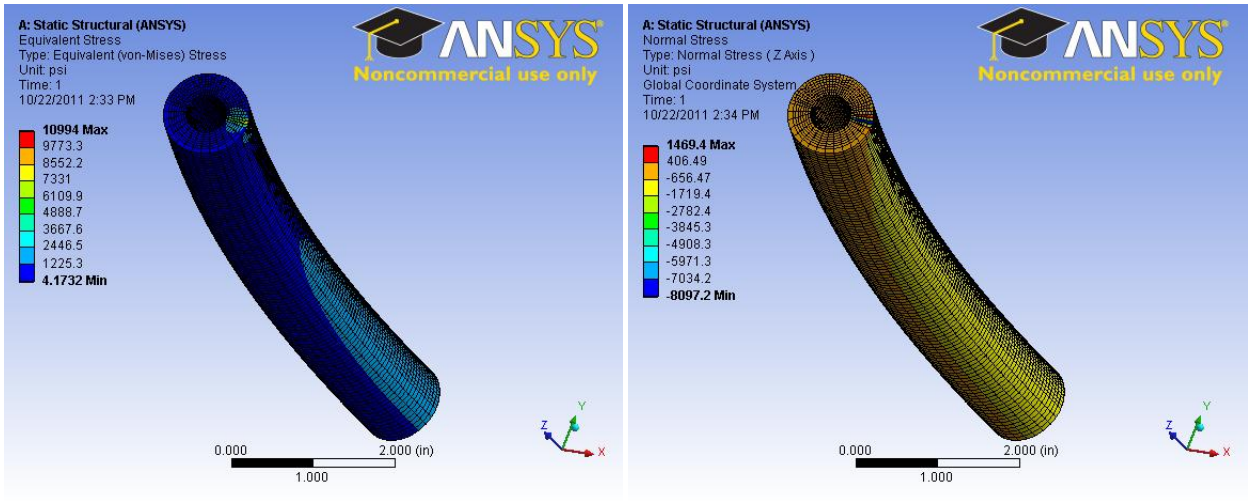

Von-Mises stress **Normal stress about z-axis**

Figure 19. Von-Mises (VM) and Normal stress distribution in the FE models of the femur under loading. Maximum stress distribution region can be observed near the mid section of the bone and close to the plane of curvature

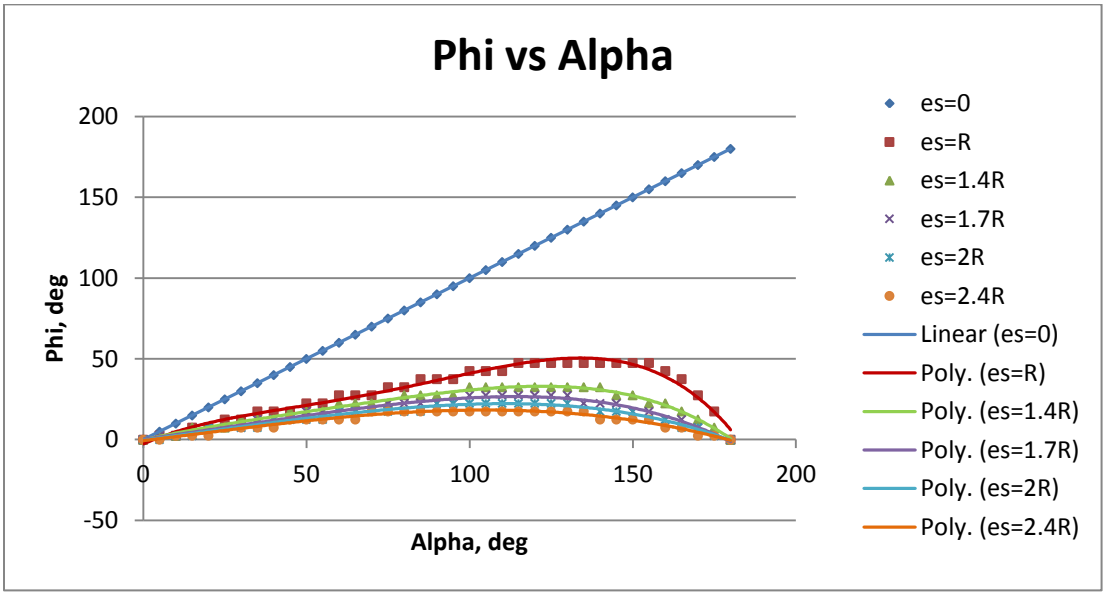

Figure 20.Phi vs. Alpha (with ANSYS results). This figure shows various sets of φ_i versus α_i values fitted with fourth degree polynomials as shown in

APPENDIX **along with the R^2 values**

As it can be seen from Fig 20, as the shape eccentricity (e_S) of the bone increases the range of ϕ reduces. Now using the range of ϕ from the fourth order polynomials, we evaluated the relative variability and then the bending predictability by following the procedure used for analytical results. Bending predictability was plotted against shape eccentricity as shown in Fig. 21.

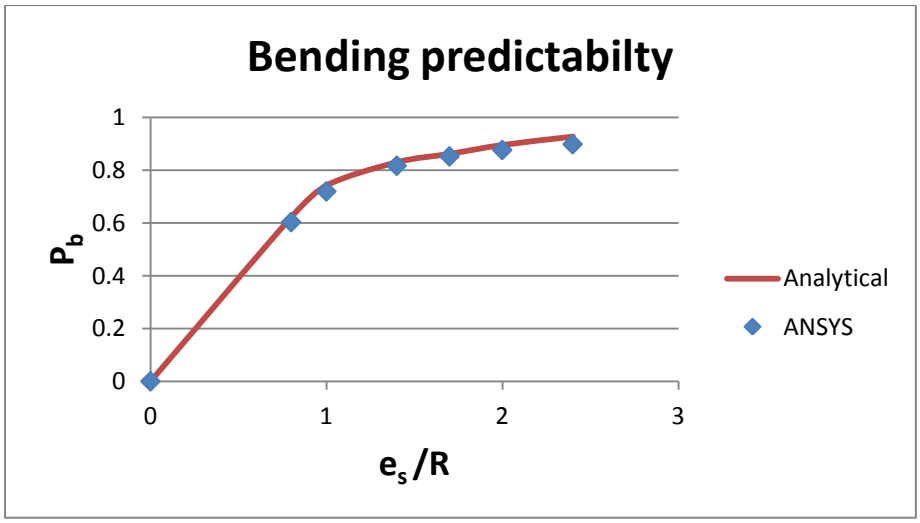

Figure 21. Bending predictability vs. Shape eccentricity (with ANSYS results)

It can be observed from Fig. 21 that there is a close resemblance in the nature of the ANSYS values obtained with the analytical curve.

3.1.2 Relative load carrying capacity by FEA results

From the simulations performed, we obtained the magnitude of maximum equivalent stress for different locations (α) of the load for different bone eccentricities. Here equivalent stress is being used instead of normal stress. This is because our task of locating the points of maximum stress is three dimensional and equivalent stress fully describes the stress state since it includes six independent stress components. Also, the equivalent stress is a good predictor for bone failure [55]. In the past analytical work discussed earlier, the authors calculated the RLCC assuming the load to be only acting in line with the curvature of the bone i.e. for α=0 deg and therefore did not consider different locations of the load while evaluating RLCC.

From the maximum stress calculated for different α values, we evaluated the relative load carrying capacity considering the different values of α. The relative load carrying capacity was calculated as follows:

$$RLCC = \frac{(\sigma_{\max})_{straight}}{(\sigma_{\max})_{curved}} \tag{11}$$

where $(\sigma_{\max})_{straight}$ is the maximum equivalent stress in a straight bone and $(\sigma_{\max})_{curved}$ is the maximum equivalent stress in a curved bone.

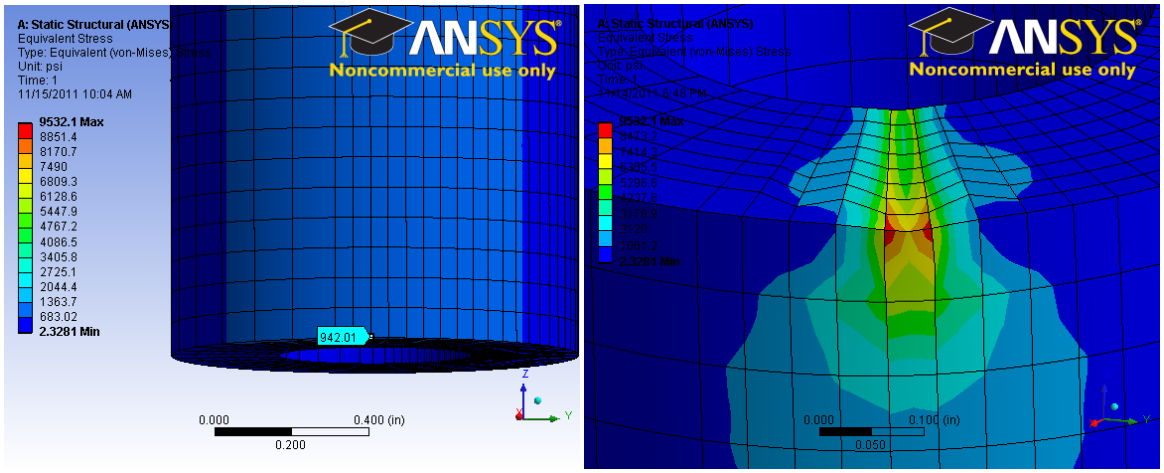

Maximum stress at mid-section Stress concentration region at the load location

Figure 22. Maximum Von-Mises stress occurring at the mid section and stress concentration region at the load location

The maximum stress occurred at the mid-section of the bone as expected, ignoring the stress concentration region around the point of application of load as shown in Fig. 22.RLCC was calculated and plotted against bone eccentricity for different load locations (α).

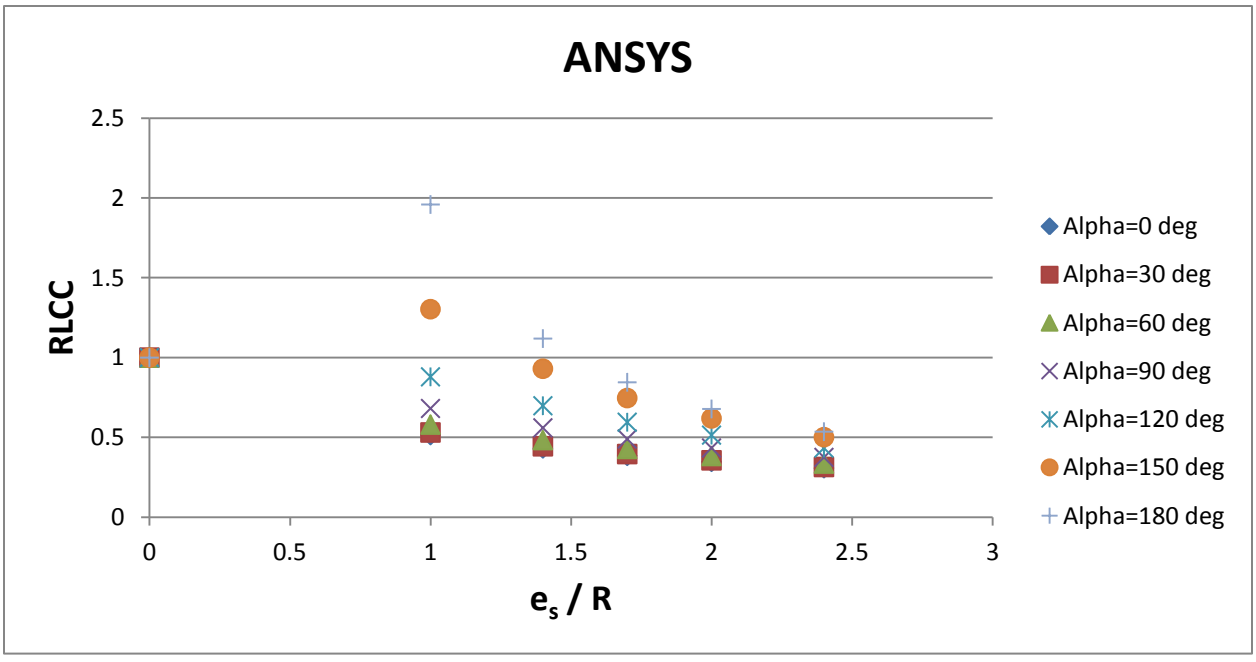

Figure 23. RLCC plotted against e_s/R for different locations of load

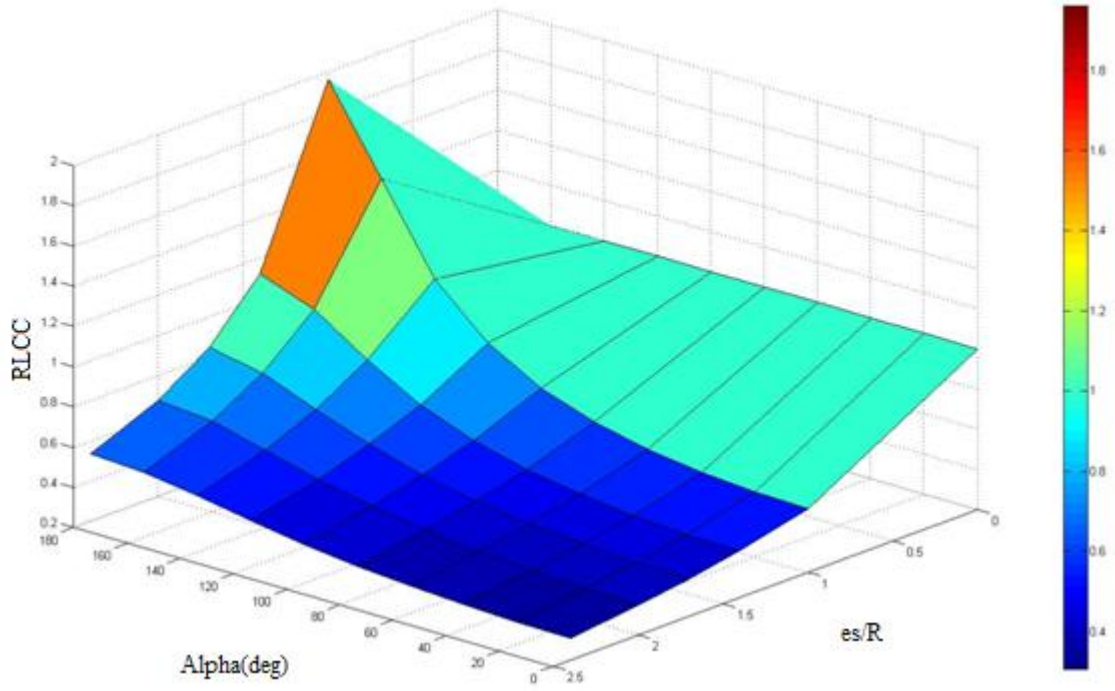

Figure 24.Surface plot of RLCC vs. Alpha vs. es/R. It can be observed that the lowest RLCC occurs when e_S is maximum and α=0 deg and RLCC increases with increase in α and with decrease in e_S.

It can be seen from Fig. 23 that for various α values, the increase in shape eccentricity (e_S) causes the relative load carrying capacity (RLCC) to reduce. However, when α becomes much larger; at around 120 degrees and higher, the RLCC is found to be greater for small e_S values than for a straight bone followed by decrease in RLCC for further increase in α. This can be observed in Fig. 23 and Fig. 24. This behavior can be attributed to the reduction in the moment arm caused by large α values which results in lowering of overall bending in the bone. Also, it was observed that at any given shape eccentricity (e_S), the RLCC increases with increase in α. In other words, a curved bone is least strong when the load is applied in the plane of curvature (α = 0 degrees). The plane of curvature in a femur is perpendicular to the femoral neck. Moving the

load off of the bone's plane of curvature reduces the eccentricity of the load and therefore increases the bone's RLCC.

3.1.3 Probability density functions of phi, ϕ □

The bending predictability graphs gave us a visual idea of how with the change in the bone eccentricity, the bending predictability changes. However, the bending predictability was evaluated based on the ranges of angle ϕ which does not address the frequency of occurrence of where maximum stress occurs due to randomness in the load location. Therefore, we attempted to get a mathematically more accurate bending probability with better visualization of the effect of various bone eccentricities separately. As the bone is subjected to dynamic loading, we assumed the location of the load, α to be a random variable between 0 and 180 and distributed uniformly. With the location of load randomized, we planned to get various ϕ values using the 4^{th} order polynomials generated earlier shown in

APPENDIX . Then using the ϕ values, we could generate probability density function (PDF) graphs for different shape eccentricities. We used R programming language[4] for generating the PDF graphs. R is an open source software language and environment for statistical computing and graphics. For generating a PDF curve for a bone, we firstly generated 100,000 random α values between 0 and 180, using the *runif* function in R statistical language. We check the uniformity of the generated α values by generating a histogram of α values and confirmed its uniformity. We then took the fourth order polynomial equation of ϕ vs. α that we got earlier and using the 100,000 random α values we generated 100,000 ϕ values. With these ϕ values, we generated a histogram of over 100 bins using the *hist* function in R statistical language. Now we calculated the x and y coordinates for the PDF. For the x coordinates we calculated the bin width and for every consecutive x coordinate, kept adding the bin width to it. For y coordinates, we calculated the frequency values from the histogram. Then, we divided each frequency value by the sample size (100,000) to get probability and then divided the probability by the bin width to get probability density. The x and y coordinates were then plotted to get the probability density function graphs. This, procedure was repeated for five shape eccentricities to get five PDF graphs shown in Fig. 25.

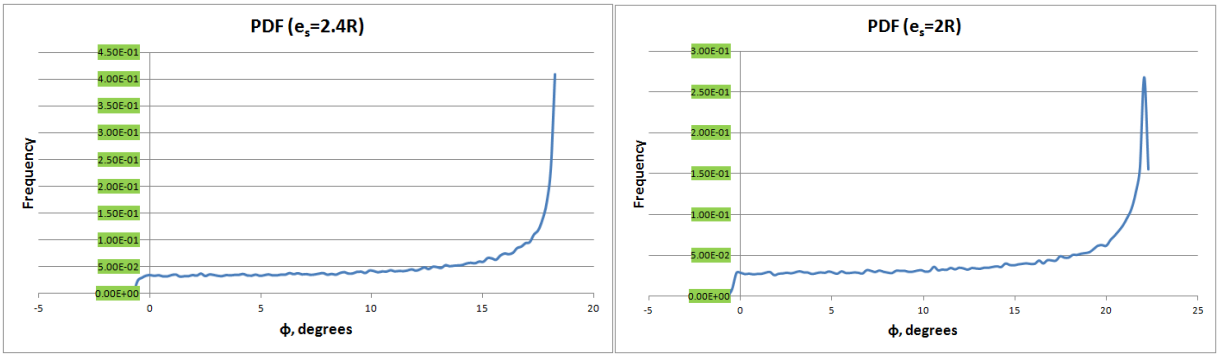

[4] R® is a product of R Development Core Team, University of Auckland, New Zealand.

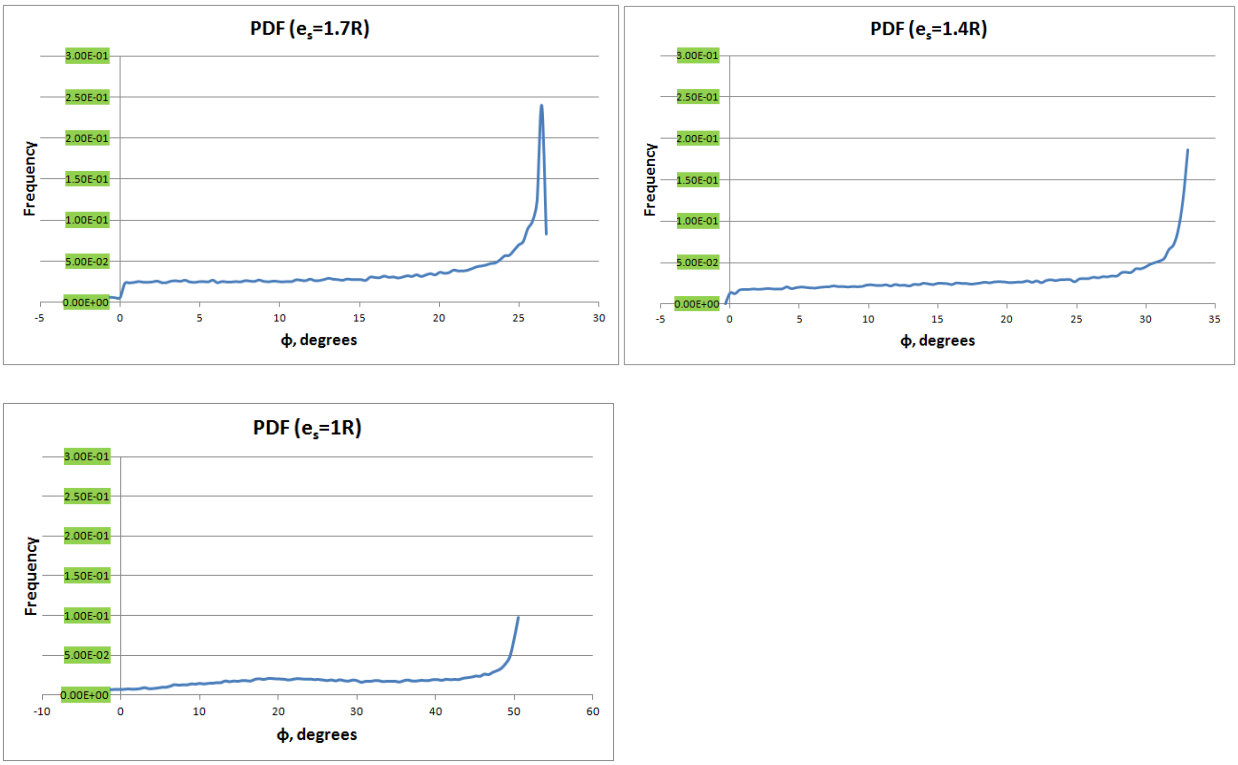

Figure 25. Probability density function curves of 'Φ' for (a) e_s=2.4R, (b) e_s=2R, (c) e_s=1.7R, (d) e_s=1.4R, (e) e_s=R

It can be observed from the probability density function graphs, as the bones' shape eccentricity increases the range of ϕ become narrower and the maximum probability density gets concentrated to smaller ranges of ϕ. Hence we can say, with increase in bone eccentricity (and bone curvature) the bending direction of the bone becomes more predictable. In other words, the probability of the bone to bend in a certain direction increases with the increase in bone eccentricity. A summary of Fig. 25 can be shown in Table 5. We can observe in Table 5 that as the bone gets more curved, the most expected location for the bone to bend gets closer to the plane of curvature.

Table 5.Summary of PDF's.

e_s	Range of Φ, deg	E (Φ), deg
1R	50.4906587	31.05

1.4R	32.98830003	25.94
1.7R	26.72878143	17.19
2R	22.30729035	14.45
2.4R	18.25435467	11.28

3.2Remote force analysis

In the previous sections, we validated the results of Bertram and Biewener [5] and then also evaluated a more comprehensive probability density function graphs for a range of shape eccentricities of femur. However, the loading on a femur is more complicated than simple normal loads as demonstrated earlier. Therefore, in this section a more realistic loading is applied to the femur CAD model. Here, we applied remote loads to simulate the joint reaction force acting on the femur head which is not part of the CAD model. In ANSYS Workbench Mechanical, remote force feature allows us to apply a force on a point, edge or face with the origin of force anywhere in the space by specifying the x, y, z coordinates of the force in space. The location of the force origin in space was calculated using geometry provided in [11] as shown in Fig. 26 and applying trigonometry and geometric relations.

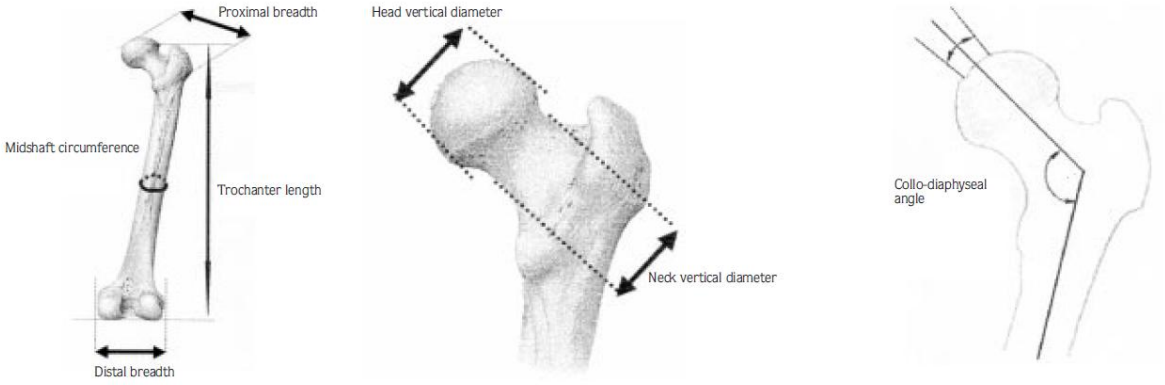

Figure 26. Femur geometry [16, 17] used to find force origin for remote force application.

After calculating the force origins, remote forces were applied at various locations in an arc shaped path, as shown in Fig. 27. This was done for different bone shape eccentricities. For each bone eccentricity and load location, a simulation was carried out and the location of maximum von Mises stress was evaluated. Fig. 27 shows the load path that was followed.

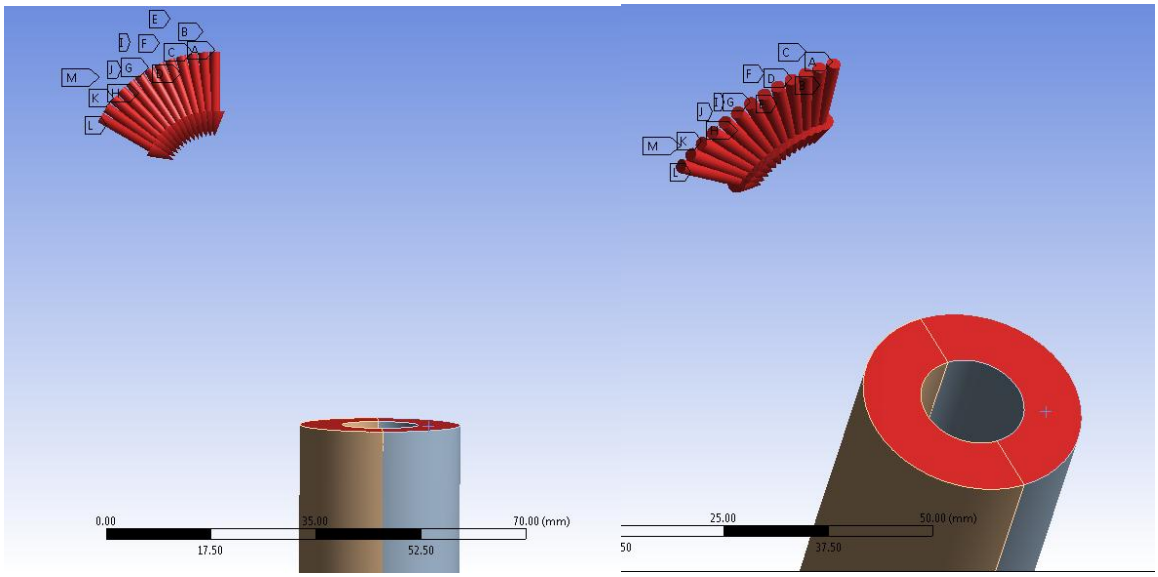

Figure 27.Remote force acting at various locations on the femur CAD model. Note that in the above figure, each arrow represents a separate load case.

The orientation of the force was calculated based on the angles β and γ as shown in Fig. 28. The expressions for force components evaluated based on angles β and γ are as follows.

$$F_x = -F \sin\beta \sin\gamma \tag{12}$$

$$F_y = -F \cos\beta \tag{13}$$

$$F_z = -F \sin\beta \cos\gamma \tag{14}$$

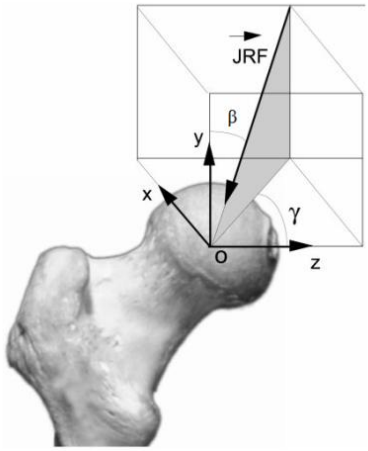

Figure 28.3D orientation of the force acting on the femur. JRF (Joint Reaction Force) makes angle β in the medial lateral plane and angle Φ with the anterior posterior plane. This is the back view of a left femur. [56]

As shown in Fig. 28, β is the angle that the force makes in the medial-lateral plane with the longitudinal axis or the y axis and γ is the angle that the force makes in the x-z plane with the z axis. Angle γ is not very significant and was therefore kept constant at 3 degrees. Angle β was varied from 0 to 30 degrees in steps of 2 degress. The location of maximum stress, ϕ was evaluated for different β values and this was repeated for different bone's shape eccentricities (e_s/R) from 0.8R to 2.4R. The table with ϕ values evaluated for different β and e_s/R values is shown in APPENDIX D.

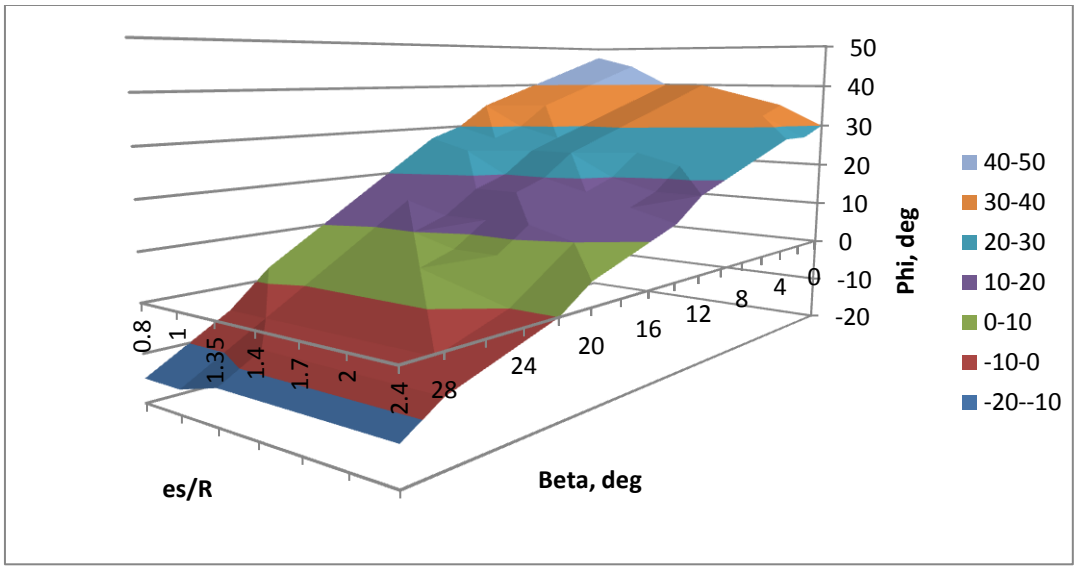

Figure 29.Surface plot of Φ vs. β vs. e_s/R. It can be observed, Φ reduces with increase in β and e_s/R.

After performing simulations for various values of β and e_s/R, the ϕ values evaluated were plotted against β and e_s/R. As it can observed from the surface plot in Fig. 29, with the increase in β and increase in e_s/R, ϕ reduces. This further shows that the range of ϕ reduces with the increase in both the e_s/R as well as β. Then, from this surface plot, we generated a quadratic equation of ϕ in terms of β and e_s/R. Using the quadratic equation we evaluated probability density function for ϕ using R language. We first generated 100,000random β values between 0 and 30 using the *rtnorm* command in R, which generates random variables within a truncated range which are normally distributed. Then we generated 100,000 random e_s/R values between 0.8 and 2.4 using the *runif* command which has the same function as that of *rtnorm* except that the resulting data is uniformly distributed. We selected uniform distribution for e_s/R because we assumed equal probabitlity of e_s/R occuring anywhere in that range. Also, a truncated normal distribution was selected for β with the mean value equal to 13 deg because we wanted β to be in the range of 0-30 deg and with the highest probability of β at 13 deg, based on

[57]. The truncated part is to limit the range to 0-30 deg. The values of β and e_s/R obtained were then substituted in the quadratic equation to obtain 100,000 values of ϕ. Using the ϕ values obtained, we generated a histogram and then a probability density function graph (see Fig. 30) following the same procedure as explained in the previous chapter.

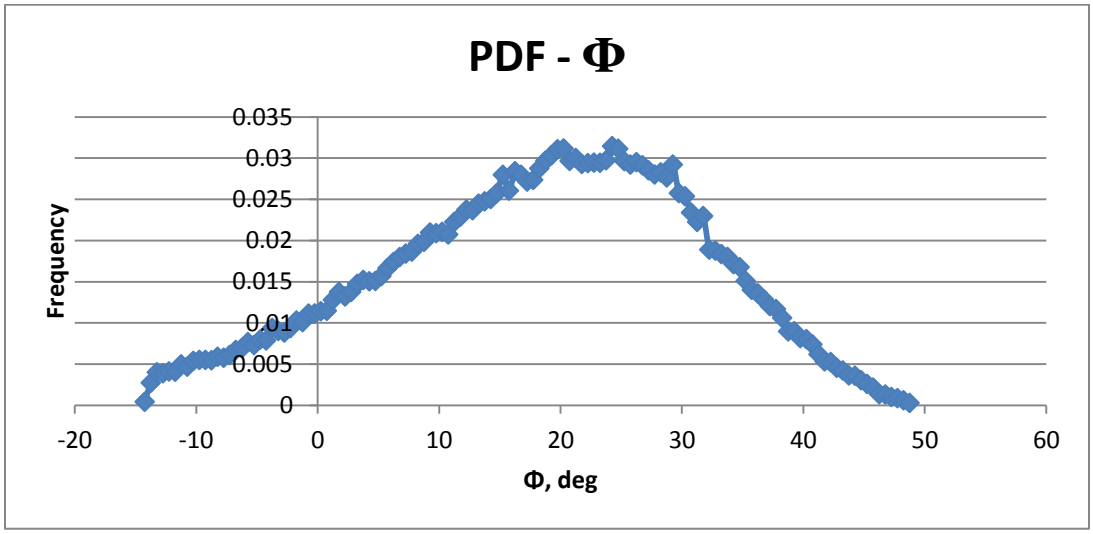

Figure 30. Probability density function curve of Φ

From Fig. 30, we can see that the maximum frequency of occurrence for ϕ is roughly in the range 20-28 degrees. Using the PDF of ϕ, the mean or expected value of ϕ was calculated using the formulae,

$$E[\phi] = \int_{-\infty}^{\infty} \phi PDF(\phi)\, d\phi \tag{15}$$

Using the limits as min(ϕ) and max(ϕ) in the above expression and solving we found

$$E[\phi] \sim 20\,\text{deg}$$

Now, we generated the probability density function graphs for each bone shape eccentricity using the same procedure as explained in section 3.1. For generating the PDF's, the ϕ vs β values generated (See APPENDIX D) were fit with fourth ordered polynomial functions and the

polynomial functions were used to generate the PDF's. The fourth ordered polynomials generated are given in APPENDIX F.

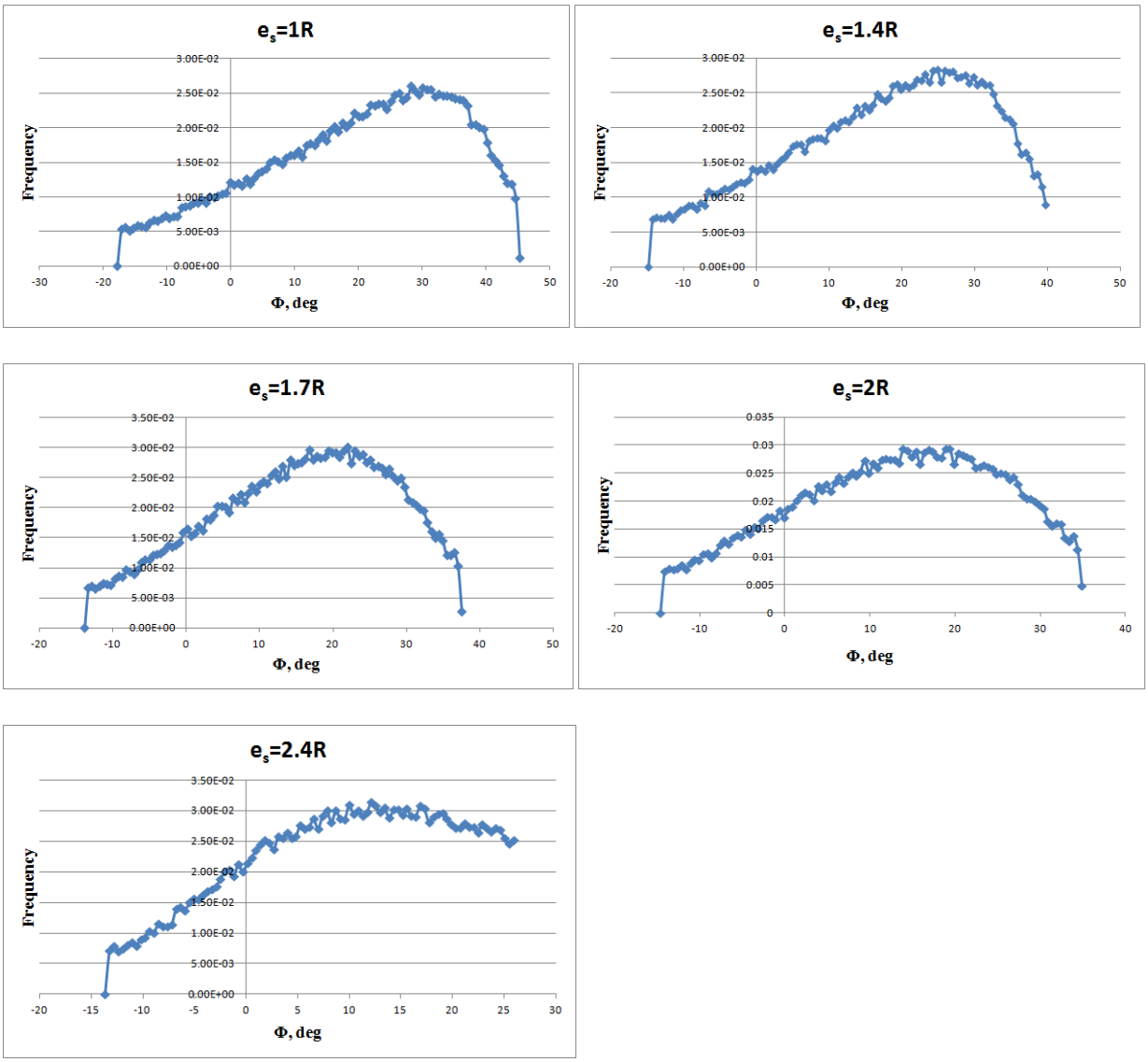

Figure 31.Probability density function curves of 'Φ' using remote forces for (a) e_s=2.4R, (b) e_s=2R, (c) e_s=1.7R, (d) e_s=1.4R, (e) e_s=R

A summary of Fig. 31 is shown in Table 6. We can observe in Table 6 that as the bone gets more curved, the most expected location for the bone to bend gets closer to the plane of curvature and the range of ϕ gets smaller.

Table 6.Summary of PDF's based on remote forces.

e_s/R	Range of Φ, deg	E (Φ), deg
1	63	19.52
1.4	54.45	16.83
1.7	51.48	14.71
2	49.5	12.69
2.4	39.56	8.5007

Now, in order to validate these results, in chapter 5 we analyzed a CT scanned model of a real human femur.

CHAPTER 4

COMPARISON WITH THE ANALYTICAL MODEL

4.1 Validation of Euler Bernoulli Beam Theory

The study by Bertram & Biewener was entirely carried out analytically using elementary mechanics. For load carrying capacity they used the 'Euler Bernoulli beam theory'. Euler Bernoulli beam theory or commonly known as the beam theory is a simplification of the linear isotropic theory of elasticity, and it can be used to calculate the relative load carrying capacity and deflection of beams. A beam can be defined as a structural element or a bar that is capable of taking loads and withstanding the load by resisting bending. The load acting could be an external load or the beam's self weight. Based on the type of support, two common types of beams are simply supported beam and cantilever beam. A simply supported beam is a beam which is freely supported at both ends. A cantilever beam is a beam which is rigidly supported at one end such that it cannot rotate about that end and freely supported at the other end. In case of curved beams, a modified Euler-Bernoulli theory has been developed for more accurate values of stress. This is because in the case of bending loading in curved beams, the neutral axis shifts inward towards the concave surface by an amount *s* due to the different lengths of fibers on the inner and outer parts of the beam as shown in Fig.32. Therefore the neutral axis and the centroidal axis of the section are not one in the same, as is the case for straight beams.

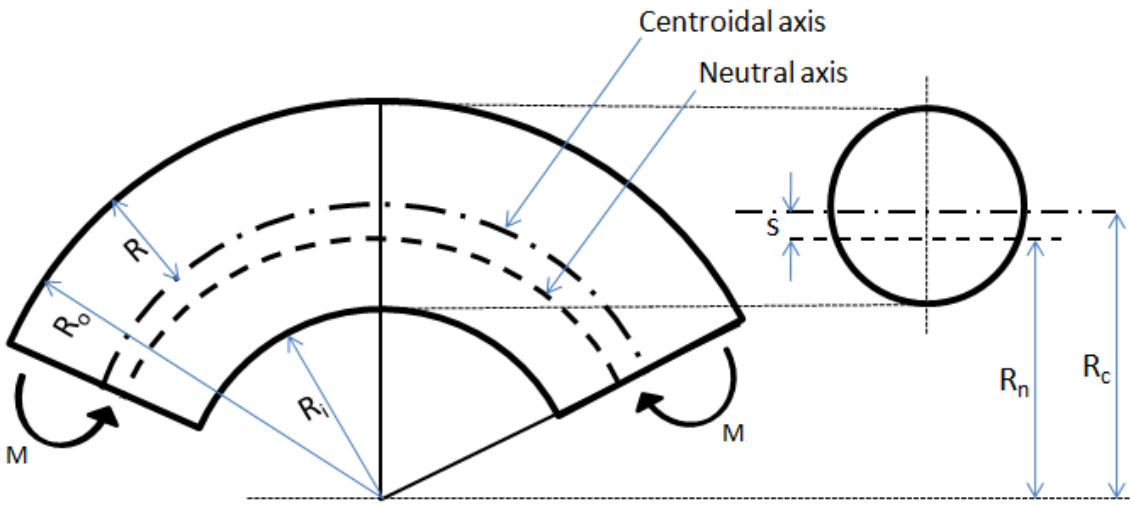

Figure 32. Curved beam under bending load. See text for definition of terms.

However, when the dimensions of the beam cross section are small compared to the radius of curvature of the longitudinal axis, the Euler-Bernoulli beam theory is relatively accurate [58, 59]. To confirm this we evaluated the 'Curvature Factor, K'. The curvature factor is defined as the multiplying factor by which the bending stress values in a straight beam are multiplied to obtain the bending stresses in a curved beam of the same section. Curvature factor, K is given by:

$$K_i = \frac{I}{sAR_i} \tag{16}$$

$$K_o = \frac{I}{sAR_o} \tag{17}$$

where K_i is the curvature factor for the inner or concave surface, K_o is the curvature factor for the outer or convex surface, I is the area moment of inertia, s is the shift of the neutral axis, A is the cross sectional area, R_i is the distance from the center of curvature to the inner surface and R_o is the distance from center of curvature to the outer surface [59].

In a curved beam bending stresses are larger in the inner or concave surface and smaller on the outer or convex surface compared to a straight beam of the same section and under the same bending moment. Hence, K_i is greater than one and K_o is less than one. Per Figure 32 the shift, s is equal to $R_c - R_n$, where R_c is the distance from the center of curvature to the centroid of the section (i.e. the bone's radius of curvature) and R_n is the radius that locates the neutral axis given by: [58, 59]

$$R_n = \frac{A}{2\pi(R_c - \sqrt{R_c^2 - R^2})} \tag{18}$$

where R is the radius of bone cross section. The derivation for the expression of R_n shown in Eq. (18) is given in APPENDIX A. The area moment of inertia (I) for a circular cross-section is given by:

$$I = \frac{\pi R^4}{4} \tag{19}$$

Here we considered the bone to be solid instead of hollow to compare to the study performed by Bertram & Biewener [5] where they considered the bone to be solid. Curvature factors were then calculated for various values of radius of curvature R_c (see Table 7). We used the R_c values from [51] where the author obtained those values from 14 human femora. Value of R used is the mean value which is obtained from femoral measurements of 72 human femora in [11].

Table 7. Curvature factor (K) calculated for the inner and outer surfaces of a curved beam

R=13.375 mm			
R_c,mm	R_c/ R	K_i	K_o
655.0223214	48.97363	1.020738	0.979887
758.7760417	56.73092	1.017864	0.982602
905.03125	67.66589	1.014945	0.985383
1125.664063	84.1618	1.011989	0.988223
1495.052083	111.7796	1.009007	0.991113
1674.97021	125.2314	1.008034	0.992062
1722.90625	128.8154	1.007809	0.992282
2236.328125	167.2021	1.006008	0.994046
4465.15625	333.8435	1.003004	0.997013

Curvature factor, K was then plotted against R_c / R as shown in Fig 33.

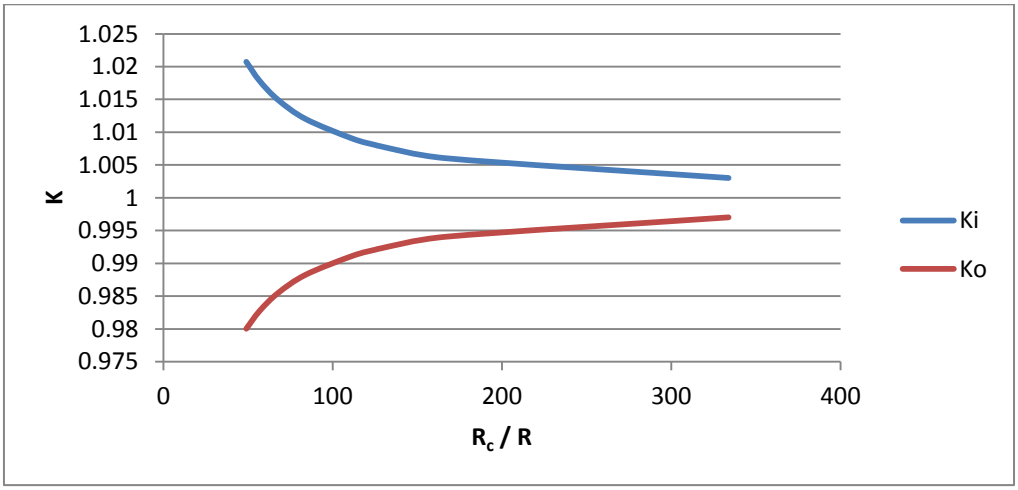

Figure 33. K_i and K_o vs. R_c / R

It can be observed from Table 7 that the values of R_c / R are very high, varying between 48 and 333 indicating very large radius of curvature values compared to the bone cross section. Also, it can be seen from the graph that the Curvature Factor, K remains almost constant close to 1. Hence, we can say that due to the large values of radii of curvature of the bone relative to the radius of the bone's cross section, the curvature effect is negligible and straight beam theory may be used with minimal error. The reader is cautioned that this curvature effect is a geometric

stress concentration effect and should not be confused with other effects of bone curvature. For example, an axial load that acts at the centroid of the end of a curved long bone will produce a bending moment on other cross sections of the curved bone, and thus bending stresses exist on these sections that normally would not be present in a straight beam axially loaded.

4.2 Analytical evaluation of bending predictability and relative load carrying capacity

In order to compare the data obtained from ANSYS results, we re-evaluated the analytical results considering the load application as per our ANSYS model. We assumed the bone to be hollow and the load to be acting on surface patches as shown in Fig 34.

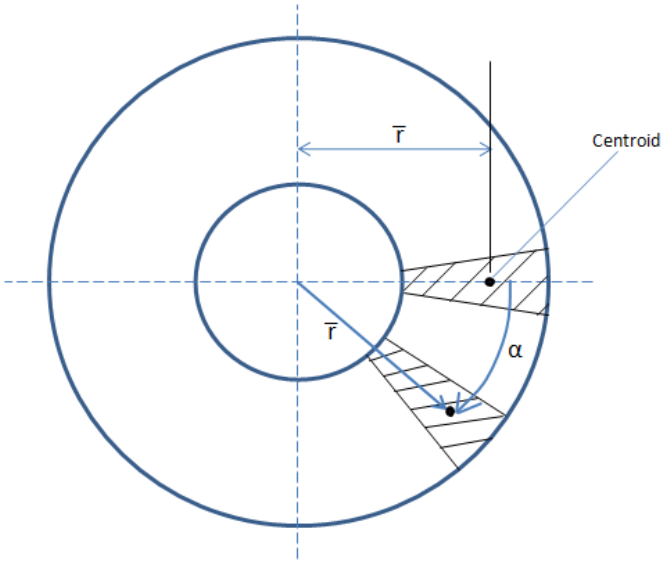

Figure 34. Top face of the bone showing the dimension, $\bar{r}$

Since we apply the load on surface patches, the load effectively acts as a point load on the centroid of the surface patch as shown in Fig. 34. Fig. 35 shows the top view of the top section and the mid-section of the bone. By applying trigonometry in Fig. 35, we get the following expression for ϕ:

$$\phi = \tan^{-1} \frac{(\bar{r} \sin \alpha)}{(\bar{r} \cos \alpha + e_s)} \tag{20}$$

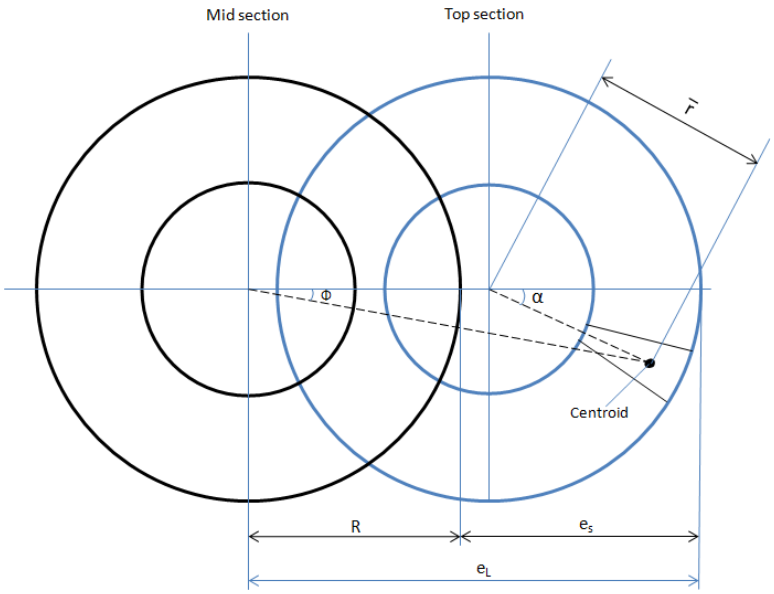

Figure 35. Top view of the top section and the mid section of the bone

where '$\bar{r}$' is the distance from the centroid of the surface patch to the center of the cross section. Again ϕ was calculated for various α values and this is repeated for different bone eccentricities. The values of ϕ were then plotted against the values of α for various shape eccentricities (e_S) of the bone.

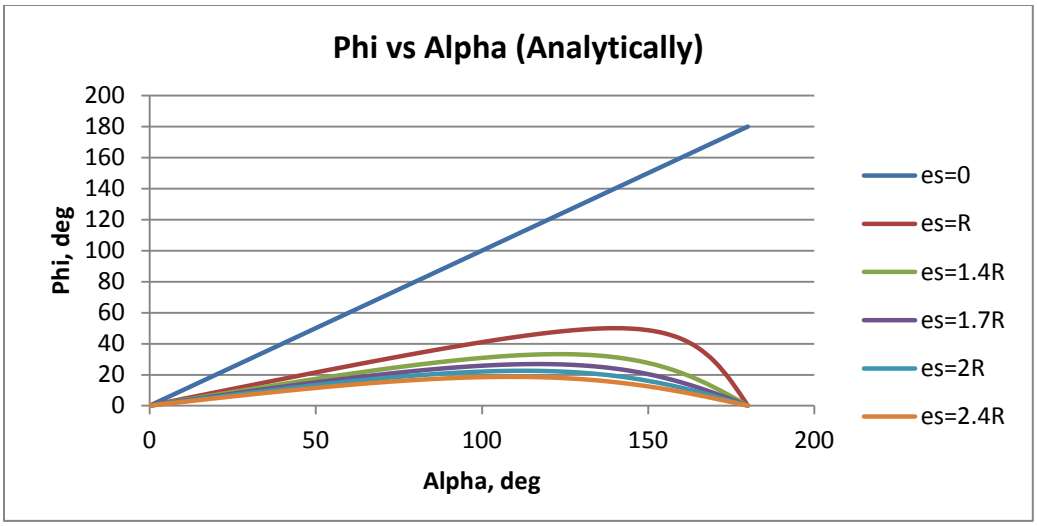

Figure 36. Phi vs. Alpha (Re-evaluated)

Calculating the range of ϕ from the above graph, we evaluated the relative variability (V_r) and from relative variability we evaluated the bending predictability using the definition of bending predictability given by Bertram & Biewener and discussed earlier in section (1.3).

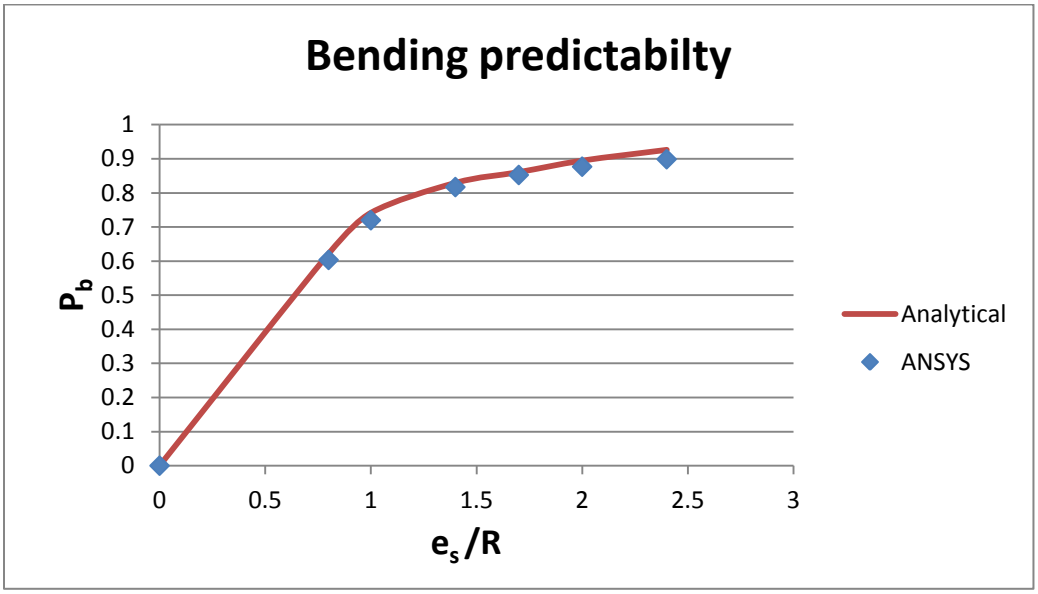

Figure 37. Bending predictability vs. Bone eccentricity

It can be observed from Fig. 37 that there is a very close similarity between the ANSYS and the re evaluated analytical bending predictability pattern. Then we compared the relative

load carrying capacity (RLCC) evaluated analytically and by ANSYS. Note that the RLCC compared here is for $\alpha = 0$ degree.

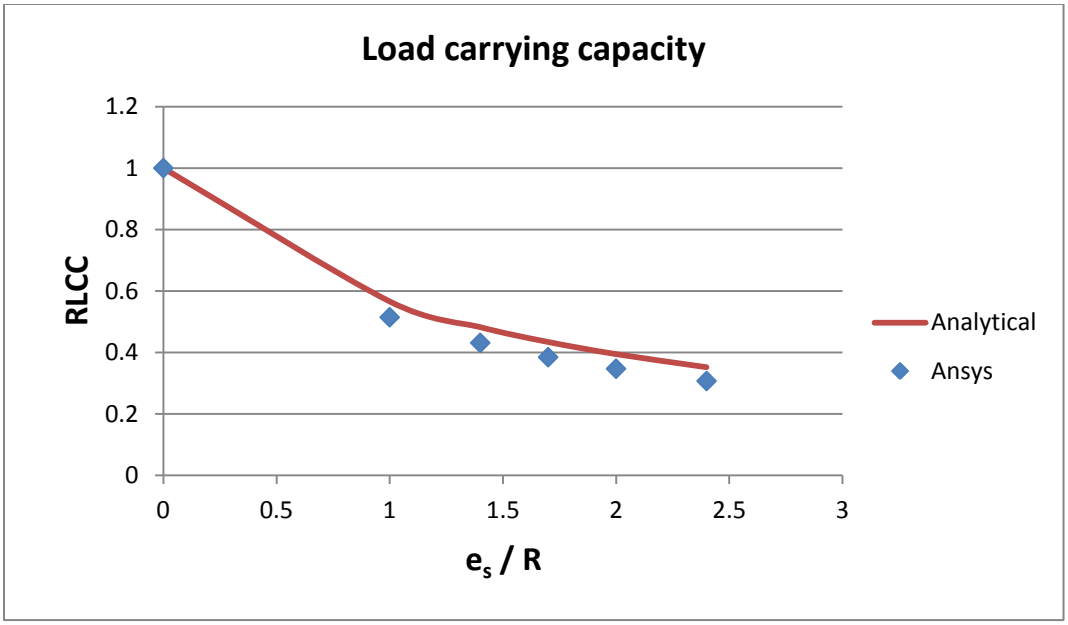

Figure 38. Comparison of RLCC vs. Shape eccentricity for ANSYS and Analytical method

There was also a very close similarity between the pattern of RLCC evaluated from ANSYS and analytically as shown in Fig. 38. In order to explain the increase in RLCC above 1 in some cases of the FEA results (see Fig.23 and Fig.24), we computed the RLCC analytically by first formulating RLCC in terms of e_s and α as follows,

$$RLCC = \left(\frac{\sigma_{Straight}}{\sigma_{Curved}} \right) \tag{21}$$

$$RLCC = \frac{\frac{F}{A} + \frac{M_s c}{I}}{\frac{F}{A} + \frac{Mc}{I}} \tag{22}$$

where $\frac{I}{c}$ is the section modulus given by $\frac{\pi(R^4 - R_i^4)}{4R}$, F is the force, A is the cross sectional area given by $\pi(R^2 - R_i^2)$, R is the outer radius, R_i is the inner radius, M_s is the moment in a straight bone given by $F\bar{r}$, M is the moment in a curved bone given by FL_m, $\bar{r}$ and L_m are the centroid distance and the moment arm respectively as shown in Fig. 39.

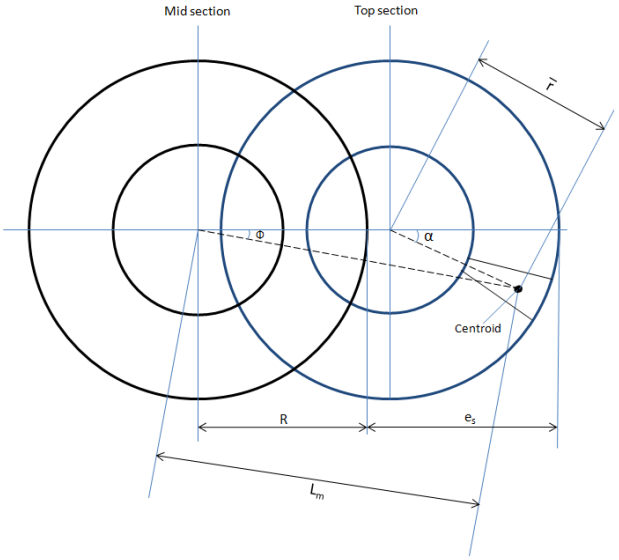

Figure 39. Top view of the top section and mid section of the bone showing the moment arm, Lm

Expression for $\bar{r}$ is:

$$\bar{r} = \frac{2(R^3 - R_i^3)}{3(R^2 - R_i^2)} \tag{23}$$

And L_m is given by

$$L_m = R\sqrt{(\frac{\bar{r}}{R}\sin\alpha)^2 + (\frac{e_s}{R} + \frac{\bar{r}}{R}\cos\alpha)^2} \tag{24}$$

The derivations for $\bar{r}$ and L_m are given in APPENDIX B. Upon substituting relevant quantities into Eq.**Error! Reference source not found.**, the following complex expression is obtained for the relative load carrying capacity RLCC:

$$RLCC = \frac{1+\frac{8}{3}\frac{R(R^3-R_i^3)}{(R^4-R_i^4)}}{1+\frac{4R\sqrt{\left(\frac{2}{3}\frac{(R^3-R_i^3)}{(R^2-R_i^2)}\sin\alpha\right)^2+\left(e_s+\frac{2(R^3-R_i^3)}{3(R^2-R_i^2)}\cos\alpha\right)^2}}{R^2+R_i^2}} \tag{25}$$

After computing RLCC mathematically for various e_s/R and α values, we plotted RLCC against e_s/R as shown in Fig. 40. We then compared the RLCC vs. e_s/R results obtained mathematically from those obtained from ANSYS results earlier.

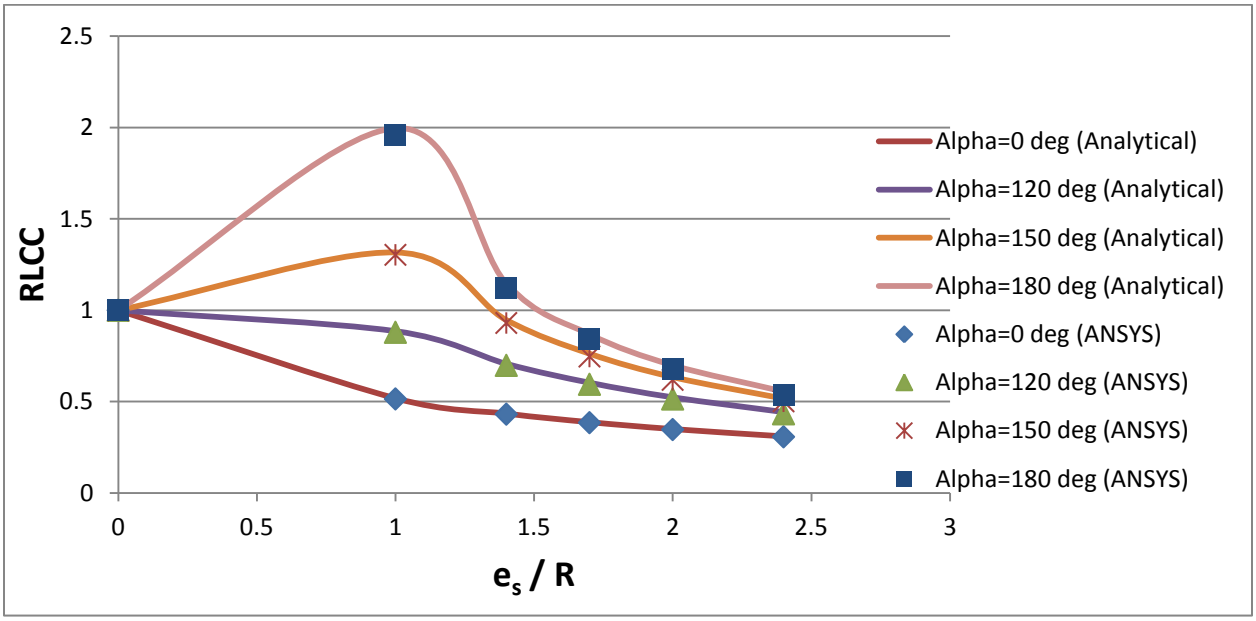

Figure 40. RLCC vs shape eccentricity from Analytical and ANSYS results

We can observe from Fig. 40 that the pattern of RLCC obtained from ANSYS results including the increase of RLCC above 1 in some cases are virtually identical to those obtained analytically for various α values. When α becomes much larger; at around 120 degrees and higher, the RLCC is found to be greater for small e_s values than for a straight bone followed by

decrease in RLCC for further increase in α. This behavior can be attributed to the reduction in the moment arm caused by large α values which results in lowering of overall bending in the bone. Overall, a very good correspondence was observed between the results obtained by Bertram &Biewener study and the results obtained from our ANSYS workbench model analysis.

CHAPTER 5

COMPARISON OF CAD AND CT SCANNED FEMUR MODEL

5.1 CT scanned femur analysis

After performing the analysis with remote forces on the femur CAD model, we wanted to compare those results to the results from a CT scanned model of a real human femur. We performed a study on a CT scanned model[5] of a real human femur to validate them. We evaluated the critical dimensions of the CT Scanned femur model. For evaluating the radius of curvature, we used the normalized curvature moment arm (NCMA) or the included angle method [53, 54]. In this method, the curve of the bone is assumed to be a part of the circumference of a circle. Based on the included angle Θ and applying geometric relations, radius of curvature was evaluated.

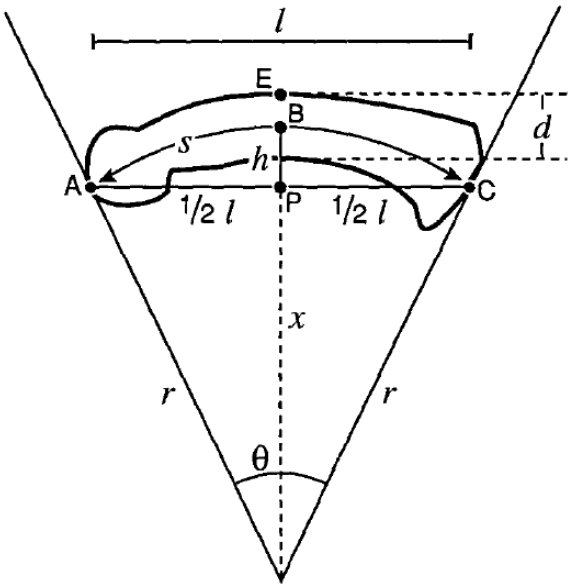

Figure 41. Landmarks and distances indicated in a phalanx (finger bone) for measuring the curvature [53]**.**

[5] The CT Scanned model of human femur was built and provided by Kelli Tamvada, doctoral candidate at the Department of Anthropology, University of Albany, NY and Professor David S. Strait, Associate professor of Anthropology, University of Albany (SUNY), NY.

Continuing the included angle method, the length, shape eccentricity and load eccentricity of the bone were calculated in Geomagic studio software[6] using the *measuring tool* present in Geomagic studio as shown in Fig. 42.

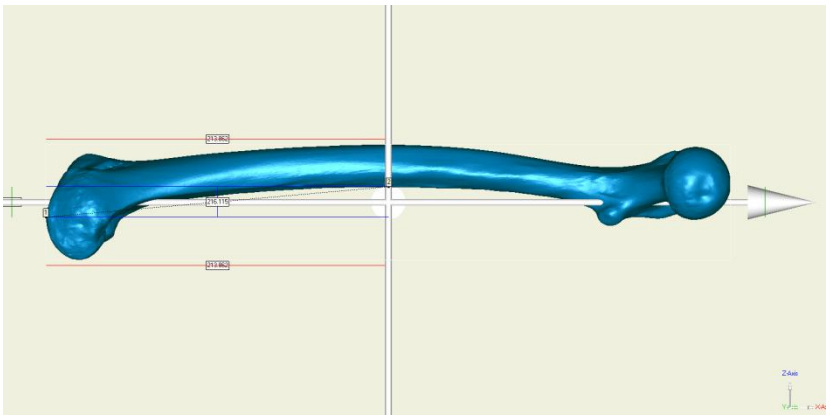

Figure 42. Side view of the CT scanned femur model in Geomagic studio for measuring dimensions.

The dimensions calculated from Geomagic studio and the included angle method were as shown in Table 8.

Table 8. Dimensions of the CT scanned femur model.

Dimension	Value, mm
Length, L	426.53
Radius, R	13.08
Shape eccentricity, e_s	17.68 (=1.35R)
Load eccentricity, e_l	30.77
Radius of curvature, R_c	754.28

[6]Geomagic Studio® is a product of Geomagic, Research Triangle Park, NC.

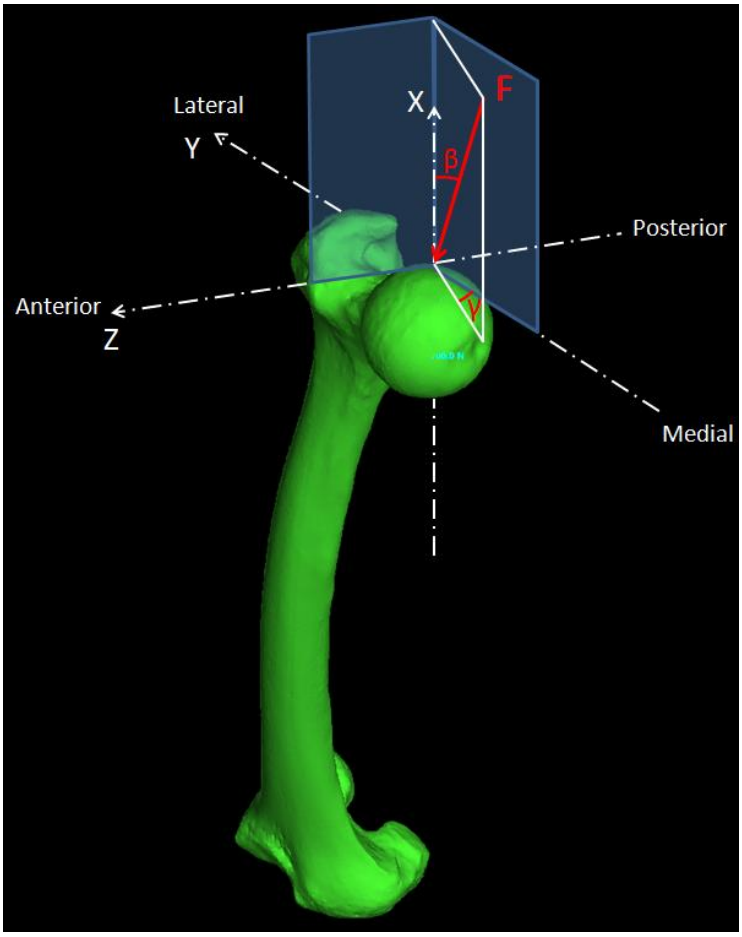

Figure 43. 3D view of the CT scanned femur model showing force orientation with angles Beta and Gamma defined as shown.

Figure 43 indicates the orientation of angle β and angle γ that defines the direction of load F.As the shape eccentricity of the femur is equal to 1.35R, the results obtained from this model were compared with the results obtained from the CAD femur model with shape eccentricity equal to 1.35R. The loads were applied on the femur head with the orientation of the load as shown in Fig. 43. Angle β was allowed to range from 0 to 30 degrees with increment of 2 degrees. For boundary conditions, displacement points were applied on the bottom face of the bone with displacement in x, y and z directions constrained as shown in Fig. 44.

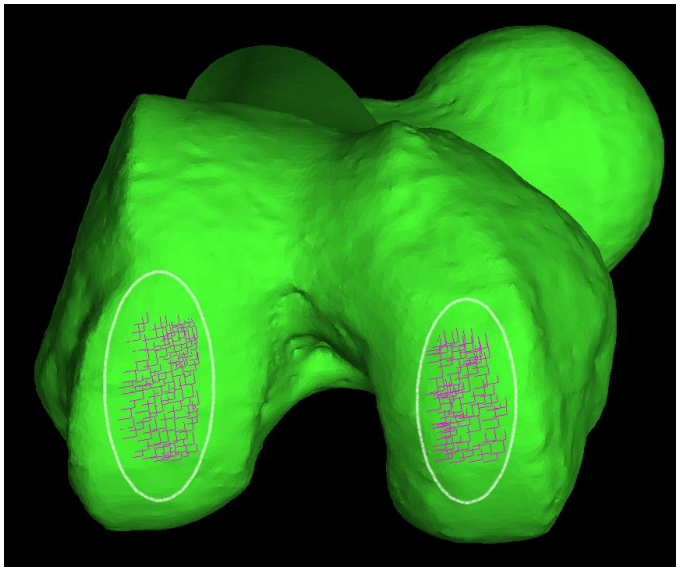

Figure 44. Displacement points applied on the bottom face of the bone. The displacement points applied are circled above.

Below, the stresses in the mid-section of the CAD model and the CT scanned femur model are compared for different β values. From Fig. 45, we can observe a good similarity in the pattern of shift of the location of maximum von Mises stress as β changes in the two models. In both the models, as β increases, the location of maximum stress moves in a similar pattern. However, there is a near constant difference in the locations of maximum stresses in the two models for all β values. This can be attributed to the axisymmetric sectional shape of the real bone.

β, degree	CAD femur model	CT Scanned femur model
0	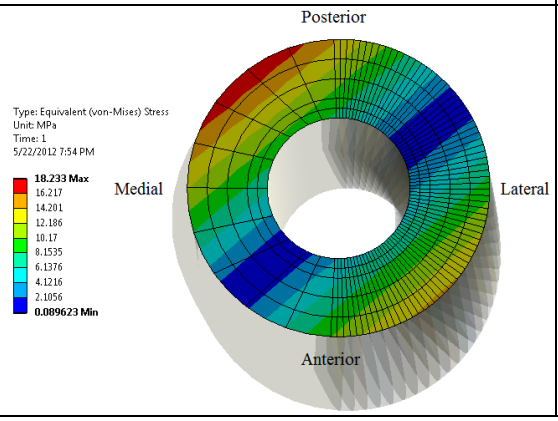	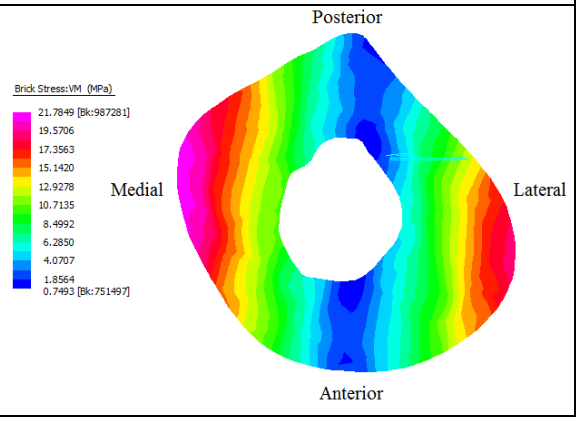

4	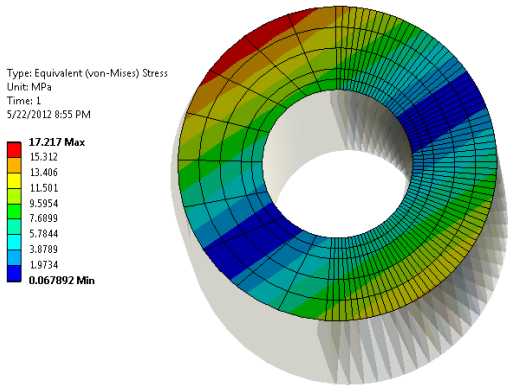 Type: Equivalent (von-Mises) Stress Unit: MPa Time: 1 5/22/2012 8:55 PM 17.217 Max 15.312 13.406 11.501 9.5954 7.6899 5.7844 3.8789 1.9734 0.067892 Min	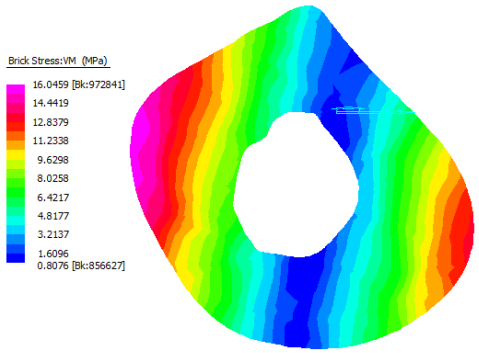 Brick Stress:VM (MPa) 16.0459 [Bk:972841] 14.4419 12.8379 11.2338 9.6298 8.0258 6.4217 4.8177 3.2137 1.6096 0.8076 [Bk:856627]
8	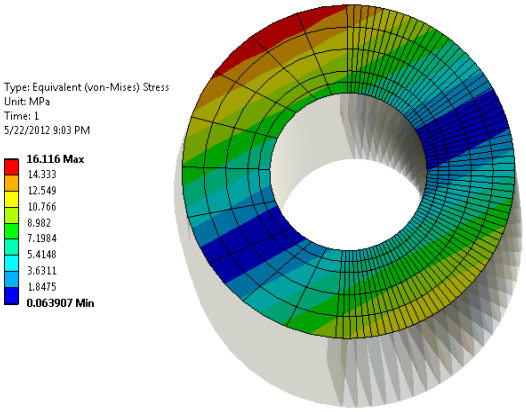 Type: Equivalent (von-Mises) Stress Unit: MPa Time: 1 5/22/2012 9:03 PM 16.116 Max 14.333 12.549 10.766 8.982 7.1984 5.4148 3.6311 1.8475 0.063907 Min	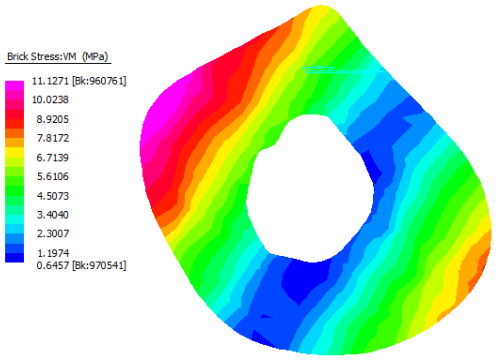 Brick Stress:VM (MPa) 11.1271 [Bk:960761] 10.0238 8.9205 7.8172 6.7139 5.6106 4.5073 3.4040 2.3007 1.1974 0.6457 [Bk:970541]
12	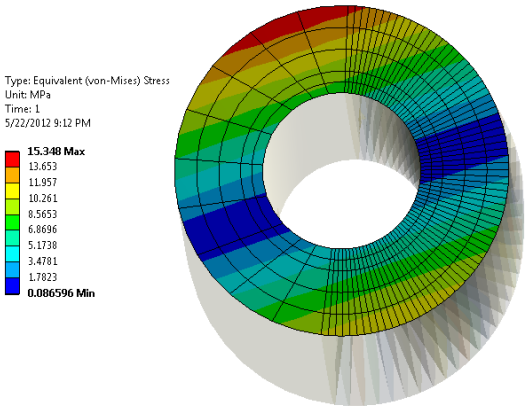 Type: Equivalent (von-Mises) Stress Unit: MPa Time: 1 5/22/2012 9:12 PM 15.348 Max 13.653 11.957 10.261 8.5653 6.8696 5.1738 3.4781 1.7823 0.086596 Min	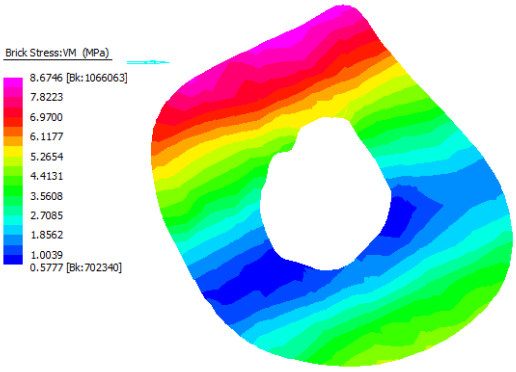 Brick Stress:VM (MPa) 8.6746 [Bk:1066063] 7.8223 6.9700 6.1177 5.2654 4.4131 3.5608 2.7085 1.8562 1.0039 0.5777 [Bk:702340]

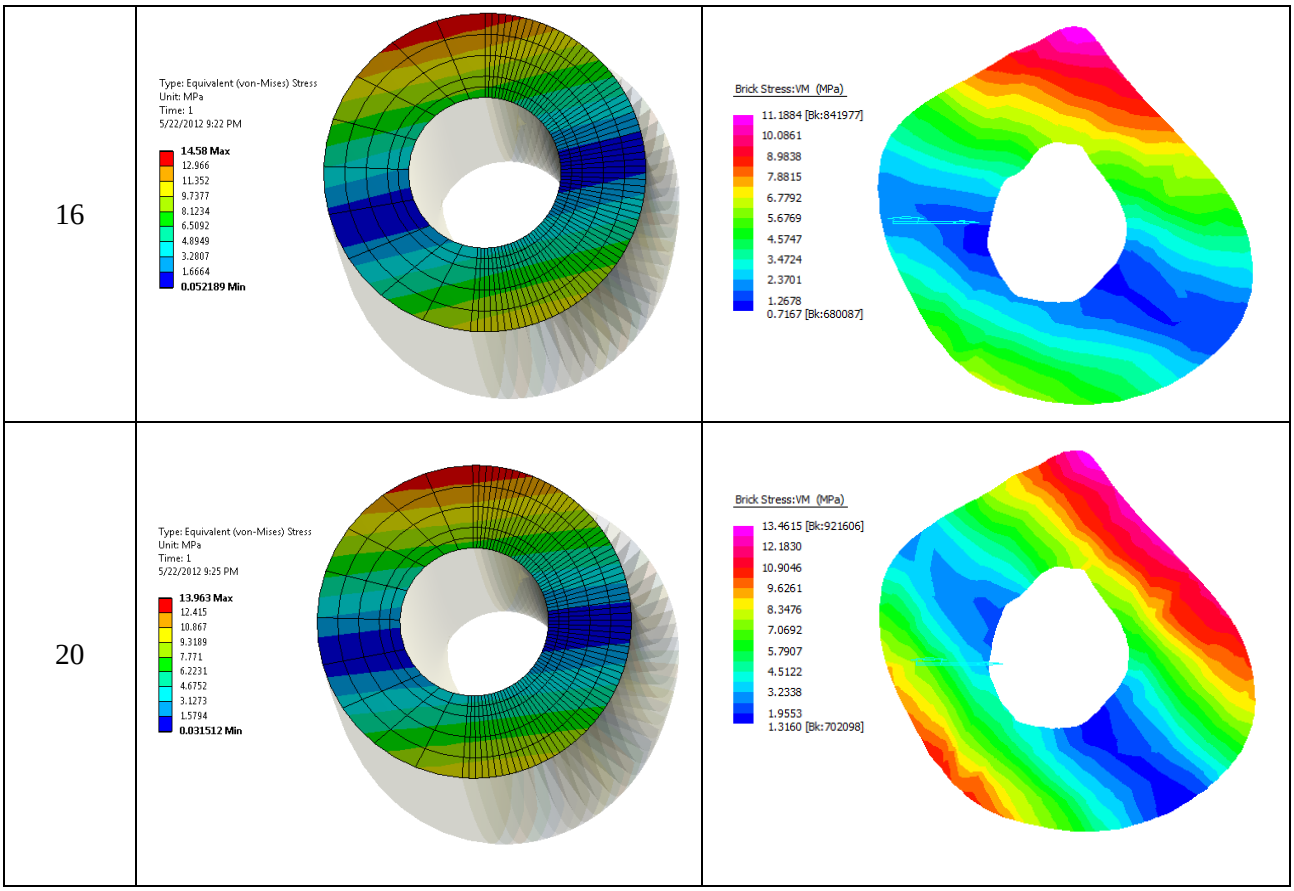

Figure 45. Von Mises stress distribution in the mid section of the CAD femur model and CT scanned femur model for different β values.

Simulations were carried out for differentβ values and various ϕ values were evaluated for the different cases. A comparison of the ϕ values obtained from the two models is shown in Table 9 and Fig. 46.

Table 9. Phi values evaluated for different beta values for the two models.

β (deg)	ϕ, CT Scanned model (deg)	ϕ, CAD model (deg)
0	83.49	40
2	79.23	37.5
4	75.76	35
6	68.98	32.5
8	60.89	30
10	38.52	27.5
12	26.69	25
14	4.82	20
16	-2	17.5
18	-8.5	12.5
20	-12.19	10
22	-76.008	5
24	-79.75	0
26	-81.99	-5
28	-86.008	-7.5
30	-89	-12.5

As it can be seen from the values and the graph below, the pattern of ϕ is similar in both the models. However, there is a difference in the magnitude of the values of the two models which can be accounted due to the shape difference in the two models. This is because in one hand the CAD model is a simplified femur without a femur head and also with half the actual length of the bone and on the other hand the CT scanned model is the model of a real femur. Also, it can be noticed from the graph that there is sudden drop in ϕ value at β~20 degrees. This is believed to be due to the shape of the bone.

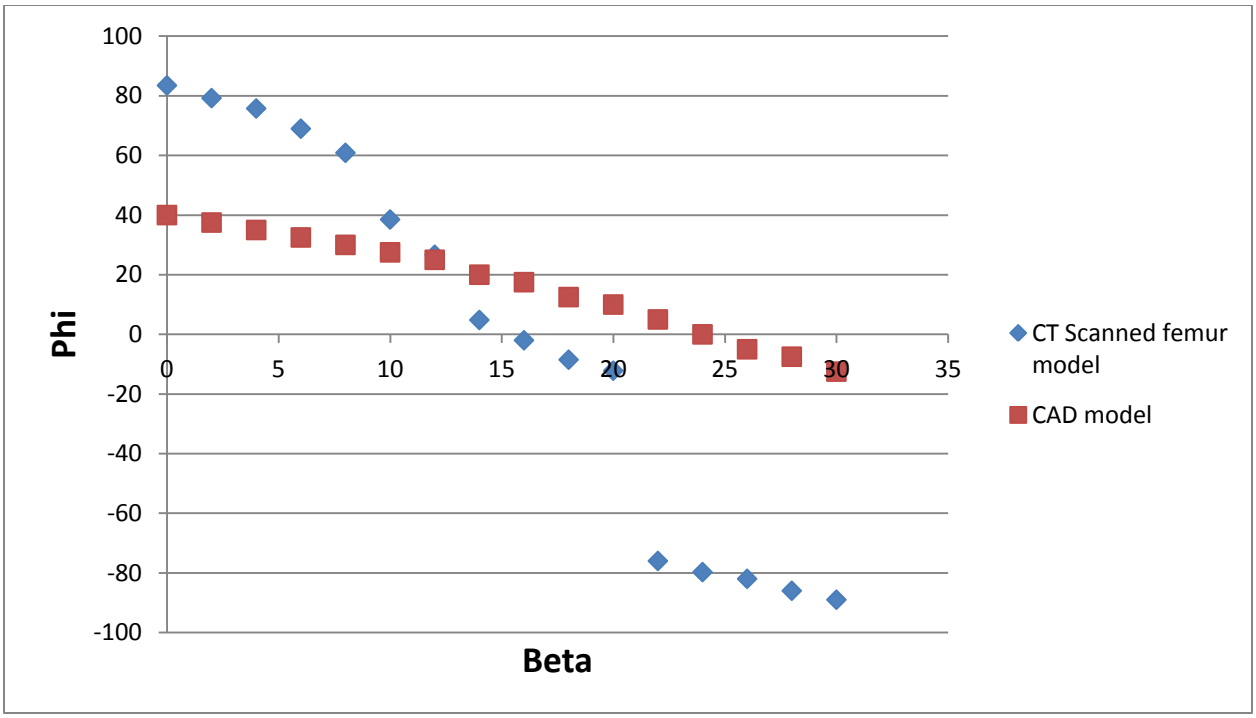

Figure 46. Variation of phi with beta for the CAD model and the CT scanned model. It can be seen that for both the models, phi reduces with increases in beta.

These points of β and ϕ obtained were then fitted with quadratic polynomials which were further used to generate probability density functions of ϕ for both the models. β was randomized between 0 and 30 degrees and then ϕ values were calculated to generate histograms and then PDF graphs (Figures 47-48), similar to the method used previously in this study.

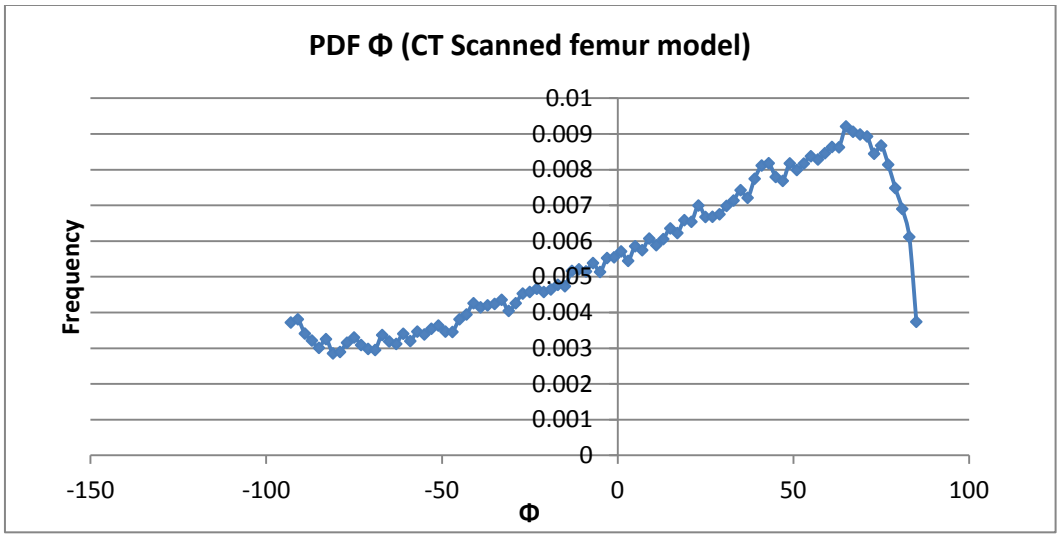

Figure 47.Probability density function graph of phi for the CT Scanned model.

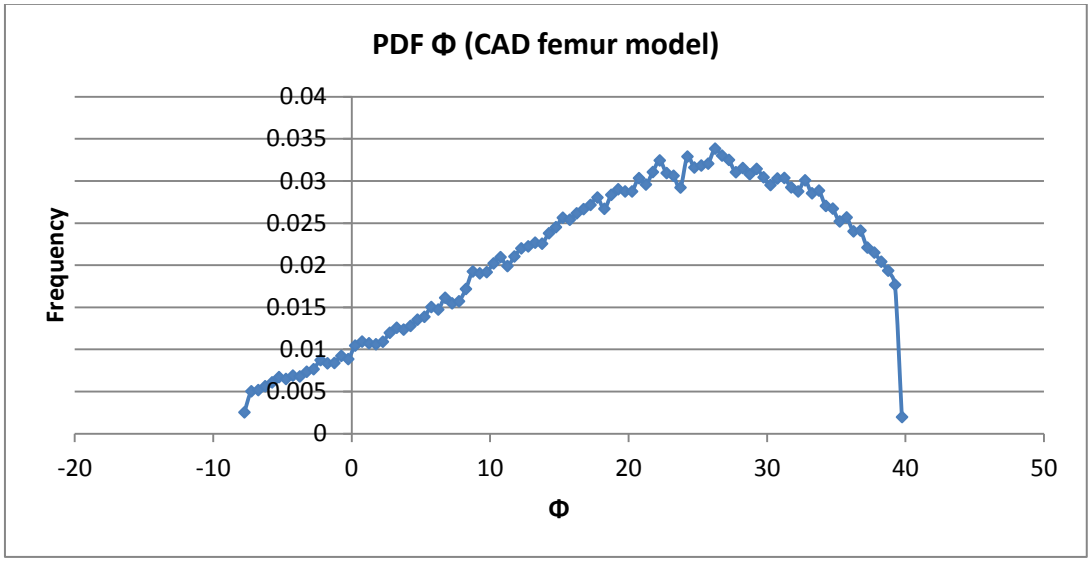

Figure 48.Probability density function graph of phi for the CAD model.

Using the PDF of ϕ and the limits of min(ϕ) and max(ϕ) the most expected value of ϕ was calculated using Eq. 15 for both the femur models:

$$E[\phi] \sim 13.03 \text{ deg (CT Scanned model)}$$

$$E[\phi] \sim 17.008 \text{ deg (CAD model)}$$

Comparing Fig. 47 and Fig. 48, we can observe that the pattern of PDF (ϕ) in both the models is very similar. This supports the result obtained from remote force analysis performed on the CAD model previously.

CHAPTER 6

RESULTS DISCUSSION

The first part of the results included the analytical results that we got after re-evaluating Bertram & Bieweners' analytical model as explained in Section 4.2. Results showed that shape eccentricity improved the bending predictability and reduced the relative load carrying capacity (see Fig.37 and Fig.38) for a load angle of $\alpha = 0$ degrees. In the second part, a CAD model was built in ANSYS Workbench Design Modeler. The results from the CAD model supported the results obtained earlier from the analytical model that the shape eccentricity improves the bending predictability at the cost of the bones' relative load carrying capacity (RLCC). However the CAD results also showed that the relative load carrying capacity at certain cases improves (see Fig.40). This happened for α equal and greater than 120 degrees and for small shape eccentricity values. This can be attributed to the reduction in the moment arm resulted due to large α values which then causes the lowering of overall bending in the bone. Therefore, as opposed to the analytical model which only showed the behavior of RLCC at $\alpha = 0$ degree, the CAD model results showed us how the RLCC behaves for different values of α from 0 to 180 degrees. This behavior was then validated by computing an expression of RLCC in terms of α and e_s. A comparison of the RLCC showed a strong agreement as shown in Fig.40. Results at this point indicated that longitudinal bone curvature present in a femur increases its bending predictability and reduces its relative load carrying capacity. Therefore bone curvature is a trade-off between bending predictability and bone strength.

In the next part, we calculated probability density functions (PDF) of ϕ for various shape eccentricities. The PDF graphs showed that as the shape eccentricity increased, the range of ϕ

and the most expected value of ϕ kept reducing and moved closer to the plane of bone curvature (see Fig.25). Therefore, the probability density function graphs proved to be a good method to estimate the most likely locations for bending in bones of varying curvature.

In the last part, we compared the results obtained from performing remote force analysis on the CAD model and analysis on the CT scanned femur model. On comparing the results, we found a good agreement between the patterns of maximum von Mises stress. As β increased, the location of maximum von Mises stress moved closer to the plane of bone curvature. This pattern was observed in both the models (see Fig. 45). However in the CT scanned model, when β exceeded 20 degrees, the location of ϕ was found to take sudden jump (see Table 9 and Fig. 46). This could be because of the bone's steep and straight profile in that region as shown in Fig. 49.

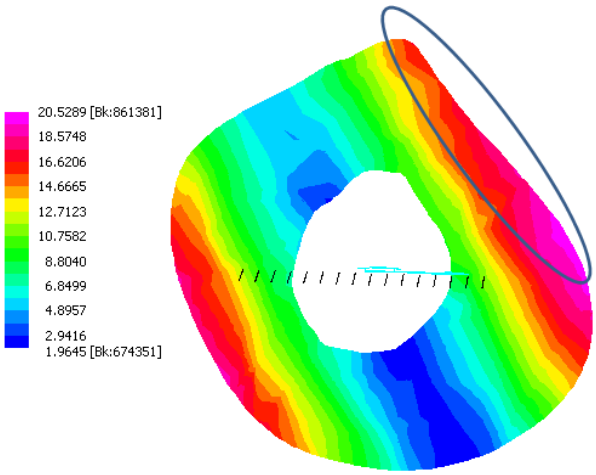

Figure 49. Section of the CT scanned femur model. The circled part shows the steep region in the cross section.

Also, the PDF of ϕ was plotted for both the models and a similar pattern was observed there too i.e. the range of ϕ was narrowed in both the cases (see Fig. 47 and Fig. 48). The most expected value of ϕ for the CAD model and the CT scanned model were evaluated to be 20.63 degrees and 13.03 degrees respectively.

CHAPTER 7

FUTURE WORK

The probability density function (PDF) graphs for ϕ that we generated are based on the assumption that α is uniformly distributed between 0 and 180 degrees. Therefore a study can be done to generate PDF graphs for ϕ by taking α to be normally distributed and check how the probability distribution for ϕ changes. We could also find data regarding how the thickness of the femur and/or its material strength changes circumferentially and longitudinally. For example, the reduction in the bone's load carrying capacity (assuming uniform material strength) due to bone curvature may be compensated by increased bone material strength in locations where bending stresses are mostly likely to be maximum based on bending predictability analysis.

Also, our work has not considered how the bone curvature effects the kinematics and kinetics of locomotion. Therefore, a study can be performed to check the kinematics and kinetics by considering the joints and muscle and also check how the stability of the knee joint is affected by bone curvature.

APPENDIX A

DERIVATION OF RADIUS OF NEUTRAL AXIS (Rn)

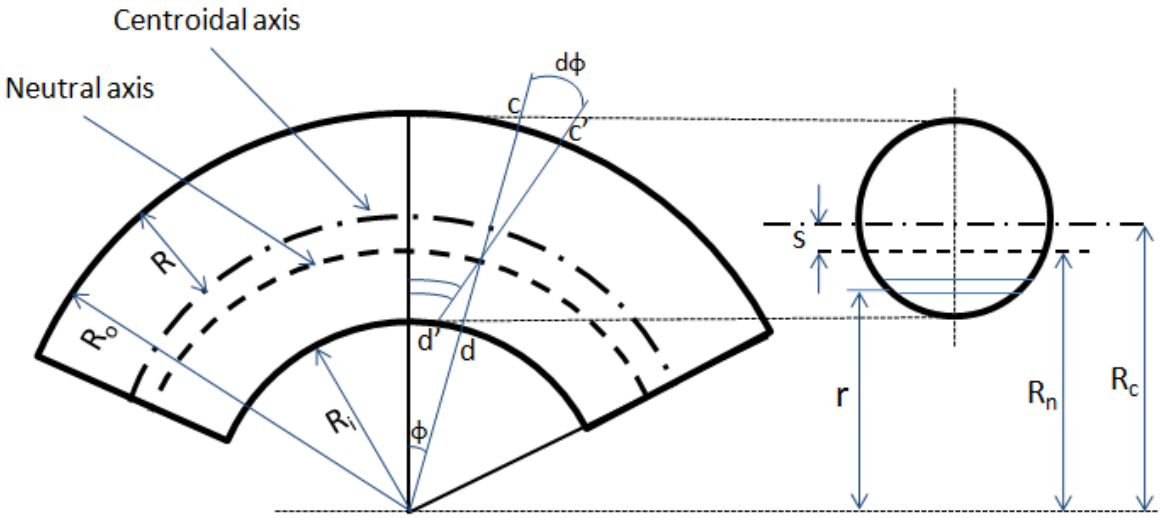

Figure 50. Curved beam in bending

Figure 50 shows a curved beam subjected to a moment. The moment causes the plane cd shown in the figure to rotate by an angle $d\phi$ to a new position c'd'. The plane cd rotates about the neutral axis. Now, consider the small fiber at a radius, 'r' which is shaded in the figure. The strain on this fiber is: [59]

$$\varepsilon = \frac{(r - R_n)d\phi}{(r)\phi} \tag{26}$$

Equilibrium of the beam requires:

$$\sum F = 0 \tag{27}$$

Now, summing the product of normal stress and the area elements over the total area:

$$\int_A \sigma dA = 0 \tag{28}$$

Also,

$$\sigma = E\varepsilon = E\frac{(r-R_n)d\phi}{(r)\phi} \tag{29}$$

$$\int_A E\frac{(r-R_n)d\phi}{(r)\phi}dA = 0$$

$$\frac{Ed\phi}{\phi}\int_A \frac{(r-R_n)}{(r)}dA = 0$$

This gives:

$$A - R_n\int_A \frac{dA}{r} = 0$$

$$R_n = \frac{A}{\int_A \frac{dA}{r}} \tag{30}$$

Now, for a circular cross section[58],

$$\int_A \frac{dA}{r} = 2\pi(R_c - \sqrt{R_c^{\,2} - R^2}) \tag{31}$$

Therefore using Eq. (31) in Eq. (30),

$$R_n = \frac{A}{2\pi(R_c - \sqrt{R_c^{\,2} - R^2})} \tag{32}$$

APPENDIX B

DERIVATION OF RADIUS OF CENTROIDAL DISTANCE ($\bar{r}$)

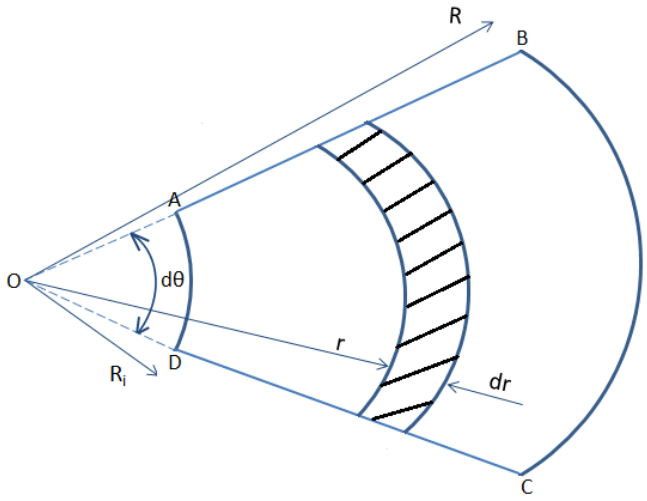

Figure 51. Centroidal distance calculated for the part ABCD.

In this part we calculate the centroidal distance for the part ABCD. ABCD is the subtraction of the sectors OBC and OAD. Consider the shaded strip with thickness dr. The centroidal distance $\bar{r}$ is given by [60]:

$$\bar{r} = \frac{1}{A}\int r dA \tag{33}$$

In our case, dA is the area of the shaded strip and A is the area of part ABCD given by:

$$A = \frac{d\theta}{2}(R^2 - R_i^{\,2}) \tag{34}$$

$$dA = r d\theta dr \tag{35}$$

Substituting A and dA in $\bar{r}$, we get:

$$\bar{r} = \frac{2}{d\theta(R^2 - R_i^{\,2})}\int_{R_i}^{R} r(r d\theta dr)$$

$$\bar{r} = \frac{2}{(R^2 - R_i^2)} \int_{R_i}^{R} r^2 dr$$

$$\bar{r} = \frac{2}{(R^2 - R_i^2)} \left[\frac{r^3}{3} \right]_{R_i}^{R}$$

$$\bar{r} = \frac{2}{3} \frac{(R^3 - R_i^3)}{(R^2 - R_i^2)} \tag{36}$$

APPENDIX C

DERIVATION OF MOMENT ARM (L_m)

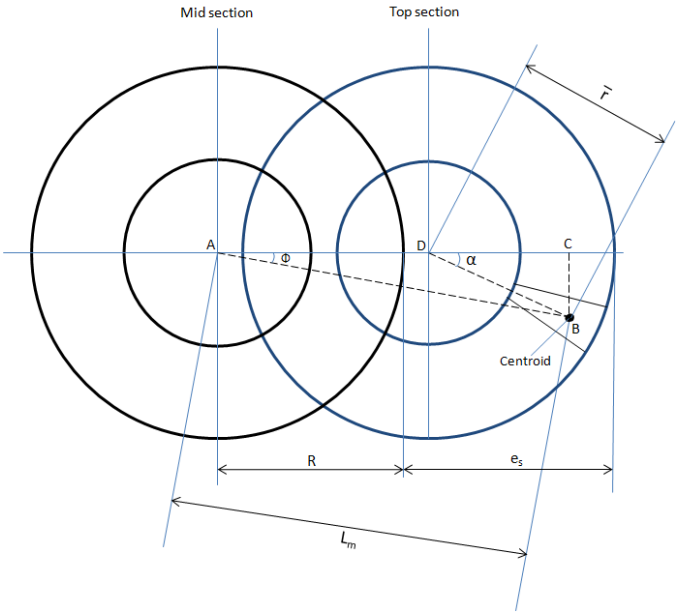

Figure 52. Top view of the top section and mid section of the bone showing the moment arm, L_m

Moment arm L_m was calculated using Pythagoras theorem in triangle ABC as shown in Figure 52.

From triangle BCD, we got:

$$BC = \bar{r}\sin\alpha \tag{37}$$

$$CD = \bar{r}\cos\alpha \tag{38}$$

Also,

$$AD = e_s \tag{39}$$

From triangle ABC,

$$(AB)^2 = (BC)^2 + (AC)^2$$

$$(L_m)^2 = (\bar{r}\sin\alpha)^2 + (AD + DC)^2$$

Using Eq.(37), Eq.(38) and Eq.(39)

$$(L_m)^2 = (\bar{r}\sin\alpha)^2 + (e_s + \bar{r}\cos\alpha)^2$$

$$L_m = \sqrt{(\bar{r}\sin\alpha)^2 + (e_s + \bar{r}\cos\alpha)^2}$$

Normalizing $\bar{r}$ using R,

$$L_m = R\sqrt{(\frac{\bar{r}}{R}\sin\alpha)^2 + (\frac{e_s}{R} + \frac{\bar{r}}{R}\cos\alpha)^2} \quad (40)$$

APPENDIX D

FOURTH ORDER POLYNOMIAL EQUATIONS GENERATED FOR FITTING φ VS. α FOR VARIOUS SHAPE ECCENTRICITIES (e_S)

e_s/ R	Polynomial equation	R^2
1	$\phi = -6E\text{-}07\ \alpha^4 + 0.0002\ \alpha^3 - 0.0147\ \alpha^2 + 0.8858\ \alpha - 2.7008$	0.9793
1.4	$\phi = -2E\text{-}07\ \alpha^4 + 4E\text{-}05\ \alpha^3 - 0.0036\ \alpha^2 + 0.4492\ \alpha - 0.1625$	0.9866
1.7	$\phi = -6E\text{-}08\ \alpha^4 + 8E\text{-}07\ \alpha^3 + 0.0002\ \alpha^2 + 0.2893\ \alpha + 0.1546$	0.9681
2	$\phi = -3E\text{-}08\ \alpha^4 - 4E\text{-}06\ \alpha^3 + 0.0001\ \alpha^2 + 0.2768\ \alpha - 0.3588$	0.9729
2.4	$\phi = 1E\text{-}08\phi^4 - 1E\text{-}05\ \alpha^3 + 0.0006\ \alpha^2 + 0.2458\ \alpha - 0.6511$	0.9621

APPENDIX E

Φ VALUES EVALUATED AGAINST β AND es/R FOR THE CAD FEMUR MODEL

	e_s/R	0.8	1	1.35	1.4	1.7	2	2.4
β	Φ							
0		47.5	45	40	40	37.5	35	30
2		45	42.5	37.5	37.5	35	32.5	27.5
4		42.5	40	35	35	32.5	30	27.5
6		40	37.5	32.5	32.5	30	27.5	25
8		37.5	35	30	30	27.5	25	22.5
10		35	30	27.5	27.5	25	22.5	20
12		30	27.5	25	25	20	17.5	17.5
14		27.5	25	20	20	17.5	15	12.5
16		22.5	20	17.5	17.5	15	12.5	10
18		17.5	15	12.5	12.5	12.5	10	7.5
20		12.5	10	10	7.5	7.5	5	5
22		7.5	5	5	5	2.5	0	0
24		2.5	0	0	0	0	-2.5	-2.5
26		-5	-5	-5	-5	-5	-5	-5
28		-10	-10	-7.5	-7.5	-7.5	-7.5	-7.5
30		-15	-15	-12.5	-12.5	-12.5	-12.5	-12.5

APPENDIX F

APDL CODE TO CALCULATE ANGLE ϕ

```
!   Commands inserted into this file will be executed immediately after the Ansys /POST1
command.

!   Active UNIT system in Workbench when this object was created:  Metric (mm, kg, N, s,
mV, mA) with temperature units of C

SET,LAST

cmsel,s,sel_face

NSORT,S,EQV,0,1,sel_face

*GET,my_n_seqv_max,SORT,0,IMAX

my_nx=nx(my_n_seqv_max)
my_ny=ny(my_n_seqv_max)
my_nz=nz(my_n_seqv_max)

my_Phi=(atan(my_ny/my_nx))*(180/3.14)
```

APPENDIX G

FOURTH ORDER POLYNOMIAL EQUATIONS GENERATED FOR FITTING φ VS. β FOR VARIOUS SHAPE ECCENTRICITIES (e_S)

e_s/ R	Polynomial equation	R^2
1	$\phi = 6E\text{-}05\beta^4 - 0.0033\beta^3 + 0.0187\beta^2 - 1.2927\beta + 45.04$	0.9994
1.4	$\phi = 6E\text{-}05\beta^4 - 0.0031\beta^3 + 0.0185\beta^2 - 1.1977\beta + 39.861$	0.9988
1.7	$\phi = 2E\text{-}05\beta^4 - 0.0011\beta^3 - 0.0012\beta^2 - 1.2177\beta + 37.5$	0.9982
2	$\phi = 1E\text{-}05\beta^4 - 0.0002\beta^3 - 0.0214\beta^2 - 1.0884\beta + 34.878$	0.9974
2.4	$\phi = -6E\text{-}05\beta^4 + 0.0044\beta^3 - 0.1205\beta^2 - 0.1525\beta + 29.408$	0.9975

BIBLIOGRAPHY

[1] C.T. Rubin, L.E. Lanyon, Limb Mechanics as a Function of Speed and Gait - a Study of Functional Strains in the Radius and Tibia of Horse and Dog, J Exp Biol. 101 (1982) 187-211.

[2] L. Lanyon, D. Baggott, Mechanical function as an influence on the structure and form of bone, Journal of Bone & Joint Surgery, British Volume. 58-B (1976) 436-443.

[3] A.A. Biewener, Allometry of Quadrupedal Locomotion - the Scaling of Duty Factor, Bone Curvature and Limb Orientation to Body Size, J Exp Biol. 105 (1983) 147-171.

[4] M. Manske, http://en.wikipedia.org/wiki/Femur, Wikipedia (2012) 1.

[5] J.E.A. Bertram, A.A. Biewener, Bone curvature: Sacrificing strength for load predictability?, J. Theor. Biol. 131 (1988) 75-92.

[6] A. Yamanaka, H. Gunji, H. Ishida, Curvature, length, and cross-sectional geometry of the femur and humerus in anthropoid primates, Am. J. Phys. Anthropol. 127 (2005) 46-57.

[7] A.A. Biewener, Bone strain: a determinant of gait and speed?, J. Exp. Biol. 123 (1986) 383.

[8] A.A. Biewener, Locomotory stresses in the limb bones of two small mammals: the ground squirrel and chipmunk, J. Exp. Biol. 103 (1983) 131.

[9] H. Frost, A Chondral Modeling Theory, Calcif. Tissue Int. 28 (1979) 181-181-200.

[10] L.E. Lanyon, The influence of function on the development of bone curvature. An experimental study on the rat tibia, J. Zool. 192 (1980) 457-466.

[11] T. Ziylan, K.A. Murshid, An Analysis of Anatolian Human Femur Anthropometry, TURKISH JOURNAL OF MEDICAL SCIENCES. 32 (2002) 231-236.

[12] Croker S.L., Donlon D., Clement J.G., A comparison of cortical bone thickness in the femoral midshaft of humans and two non-human mammals, HOMO HOMO- Journal of Comparative Human Biology. 60 (2009) 551-565.

[13] O. Panagiotopoulou, Finite element analysis (FEA): Applying an engineering method to functional morphology in anthropology and human biology, Annals of Human Biology. 36 (2009) 609-623.

[14] S. Moaveni, , in: Finite element analysis : theory and application with ANSYS, Pearson Prentice Hall, Upper Saddle River, N.J, 2008.

[15] R.D. Cook, D.S. Malkus, M.E. Plesha, , in: Concepts and applications of finite element analysis, Wiley, New York, 1989.

[16] O.C. Zienkiewicz, R.L. Taylor, The finite element method, Butterworth-Heinemann, Oxford; Boston, 2000.

[17] J.N. Reddy, C.S. Krishnamoorthy, K.N. Seetharamu, Finite element analysis for engineering design, Springer-Verlag, Berlin; New York, 1988.

[18] T.J.R. Hughes, The finite element method : linear static and dynamic finite element analysis, Dover Publications, Mineola, NY, 2000.

[19] K. Bathe, E.L. Wilson , Numerical methods in finite element analysis, Prentice-Hall, Englewood Cliffs, N.J., 1976.

[20] E.J. Rayfield, Finite Element Analysis and Understanding the Biomechanics and Evolution of Living and Fossil Organisms, Annu. Rev. Earth Planet. Sci. 35 (2007) 541-576.

[21] Prendergast PJ, Lennon AB, AN INTRODUCTION TO THE WORKSHOP ON FINITE ELEMENT MODELLING IN BIOMECHANICS AND MECHANOBIOLOGY, European Society of Biomechanics (2007).

[22] I.R. Grosse, S.A. Wood, D.S. Strait, E.R. Dumont, C.F. Ross, Response to the Comment by Gröning and Fagan on "The effects of modeling simplifications on craniofacial finite element models: The alveoli (tooth sockets) and periodontal ligaments" (volume 44, issue 10, pages 1831–1838), Journal of Biomechanics Journal of Biomechanics. 45 (2012) 1750-1751.

[23] D.S. Strait, G. Weber, P. Constantino, P.W. Lucas, B.G. Richmond, M.A. Spencer, P.C. Dechow, C. Ross , I.R. Grosse, B.W. Wright, B.A. Wood, Q. Wang, B. Craig, D.E. Slice, Microwear, mechanics and the feeding adaptations of Australopithecus africanus., J. Hum. Evol. 62 (2012) 165-168.

[24] M.A. Berthaume, P.C. Dechow, J. Iriarte-Diaz, C.F. Ross, D.S. Strait, Q. Wang, I.R. Grosse, Probabilistic finite element analysis of a craniofacial finite element model, J. Theor. Biol. 300 (2012) 242-253.

[25] Wang Q, Wood SA, Grosse IR, Ross CF, Zapata U, Byron CD, Wright BW, Strait DS, The role of the sutures in biomechanical dynamic simulation of a macaque cranial finite element model: implications for the evolution of craniofacial form., Anatomical record (Hoboken, N.J.: 2007). 295 (2012) 278-88.

[26] S.A. Wood, D.S. Strait, E.R. Dumont, C.F. Ross, I.R. Grosse, The effects of modeling simplifications on craniofacial finite element models: The alveoli (tooth sockets) and periodontal ligaments, J. Biomech. 44 (2011) 1831-1838.

[27] Benazzi S, Kullmer O, Grosse IR, Weber GW, Using occlusal wear information and finite element analysis to investigate stress distributions in human molars., J. Anat. 219 (2011) 259-72.

[28] Davis JL, Dumont ER, Strait DS, Grosse IR, An efficient method of modeling material properties using a thermal diffusion analogy: an example based on craniofacial bone., PloS one. 6 (2011).

[29] E.M. Hecht, D.M. Cullinane, I.R. Grosse, A novel stress distribution organ in the arthropod exoskeleton., Arthropod Structure & Development. 39 (2010).

[30] Davis, J. L., Santana, S. E., Dumont, E. R., Grosse, I. R., Predicting bite force in mammals: two-dimensional versus three-dimensional levermodels, Journal of Experimental Biology. 213 (2010) 1844.

[31] S. Benazzi, F. Bookstein, D.S. Strait, B. Richmond, P. Lucas, P. Dechow, C. Ross, I. Grosse, G.W. Weber, A symmetric virtual reconstruction of OH5., Am. J. Phys. Anthropol. 2010 (2010) 65.

[32] A. Smith, I. Grosse, P. Dechow, D. Strait, Representing the geometry of organisms: Precision and accuracy in finite element modeling., Am. J. Phys. Anthropol. 2010 (2010) 218.

[33] Wang Q., Zapata U., Smith A.L., Strait D.S., Wright B.W., Richmond B.G., Grosse I.R., Byron C.D., The global impact of sutures assessed in a finite element model of a macaque cranium, American Journal of Physical Anthropology. 293 (2010) 1477-1491.

[34] Strait D.S., Smith A.L., Grosse I.R., Dechow P.C., Wang Q., Weber G.W., Neubauer S., Slice D.E., Chalk J., Richmond B.G., Lucas P.W., Spencer M.A., Schrein C., Wright B.W., Byron C., Ross C.F., The structural rigidity of the cranium of Australopithecus africanus: Implications for diet, dietary adaptations, and the allometry of feeding biomechanics, The Anatomical Record. 293 (2010) 583-593.

[35] Berthaume M., Grosse I.R., Patel N.D., Wood S., Strait D.S., Richmond B.G., The effect of early hominin occlusal morphology on the fracturing of hard food items, The Anatomical Record. 293 (2010) 594-606.

[36] E.R. Dumont, I.R. Grosse, G.J. Slater, Requirements for comparing the performance of finite element models of biological structures, J. Theor. Biol. 256 (2009) 96-103.

[37] D. Strait, G. Weber, S. Neubauer, J. Chalk, B. Richmond, P. Lucas, M. Spencer, C. Schrein, P. Dechow, C. Ross, I. Grosse, B. Wright, P. Constantino, B. Wood, B. Lawn, W. Hylander, Q. Wang, C. Byron, D. Slice, A. Smith, The feeding biomechanics and dietary ecology of Australopithecus africanus, Proceedings of the National Academy of Science. 106 (2009) 2124-2129.

[38] B.G. Richmond, B.W. Wright, I. Grosse, P.C. Dechow, C.F. Ross, M.A. Spencer, D.S. Strait, Finite element analysis in functional morphology, The Anatomical Record. 283A (2005) 259-274.

[39] E.J. Rayfield, Finite Element Analysis and Understanding the Biomechanics and Evolution of Living and Fossil Organisms, Annual Review of Earth and Planetary Sciences. 35 (2007) 541-576.

[40] Rayfield EJ., Cranial mechanics and feeding in tyrannosaurus rex, Proc Royal Soc Lond B Biol Sci. 271 (2004) 1451-1459.

[41] Korioth TW, Romilly DP, Hannam AG, Three-dimensional finite element stress analysis of the dentate human mandible., Am. J. Phys. Anthropol. 88 (1992) 69-96.

[42] Rayfield EJ, Norman DB, Horner CC, Horner JR, Smith PM, Thomason JJ, Upchurch P, Cranial design and function in a large theropod dinosaur., Nature. 409 (2001) 1033-7.

[43] S. Schutte, Sven P.W. van den Bedem, F.V. Keulen, Frans C.T. van der Helm, Huibert J. Simonsz, A finite-element analysis model of orbital biomechanics, Vision Research. 46 (2006) 1724-1731.

[44] Ross CF, Finite element analysis in vertebrate biomechanics., The anatomical record.Part A, Discoveries in molecular, cellular, and evolutionary biology. 283 (2005) 253-8.

[45] E. Schileo, F. Taddei, A. Malandrino, L. Cristofolini, M. Viceconti, Subject-specific finite element models can accurately predict strain levels in long bones, J. Biomech. 40 (2007) 2982-2989.

[46] Dumont ER, Piccirillo J, Grosse IR, Finite-element analysis of biting behavior and bone stress in the facial skeletons of bats., The anatomical record. 283 (2005) 319-30.

[47] Farke A.A., Frontal sinuses and head-butting in goats: A finite element analysis, Journal of Experimental Biology. 211 (2008) 3085-3094.

[48] K. Kupczik, C.A. Dobson, M.J. Fagan, R.H. Crompton, C.E. Oxnard, P. O'Higgins, Assessing mechanical function of the zygomatic region in macaques: validation and sensitivity testing of finite element models, J. Anat. 210 (2007) 41-53.

[49] E. Munting, M. Verhelpen, Mechanical simulator for the upper femur, Acta orthopaedica Belgica. 59 (1993) 123-9.

[50] J. Carter, http://biology.clc.uc.edu/courses/bio104/intro104.htm, Welcome to General Biology 104. 2011 (2010) 2.

[51] Harper MC, Carson WL, Curvature of the femur and the proximal entry point for an intramedullary rod., Clin. Orthop. (1987) 155-61.

[52] A. Schonning, B. Oommen, I. Ionescu, T. Conway, Medical Modeling Special Issue: An Introduction, Hexahedral mesh development of free-formed geometry: The human femur exemplified, Comput. -Aided Des. 41 (2009) 566-572.

[53] Stern JT Jr, Jungers WL, Susman RL, Quantifying phalangeal curvature: an empirical comparison of alternative methods., Am. J. Phys. Anthropol. 97 (1995) 1-10.

[54] De Groote I., Lockwood C.A., Aiello L.C., Technical note: A new method for measuring long bone curvature using 3D landmarks and semi-landmarks, Am.J.Phys.Anthropol.American Journal of Physical Anthropology. 141 (2010) 658-664.

[55] J.H. Keyak, S.A. Rossi, Prediction of femoral fracture load using finite element models: an examination of stress- and strain-based failure theories, J. Biomech. 33 (2000) 209-214.

[56] Simões JA, Vaz MA, Blatcher S, Taylor M, Influence of head constraint and muscle forces on the strain distribution within the intact femur., Med. Eng. Phys. 22 (2000) 453-9.

[57] Taylor ME, Tanner KE, Freeman MA, Yettram AL, Stress and strain distribution within the intact femur: compression or bending?, Med. Eng. Phys. 18 (1996) 122-31.

[58] R. Beardmore, http://www.roymech.co.uk/Useful_Tables/Beams/Curved_beams.html, Roymech. co. uk. 2011 (2010) 1.

[59] R. Juvinall, K. Marshek, Pure Bending Loading, Curved Beams, in: Fundamentals of Machine Component Design, John Wiley & Sons, United States of America, 1991, pp. 107-108,109,110.

[60] R.W. Soutas-Little, D.J. Inman, D.S. Balint, Centroids of Areas, Volumes, and Lines; The First Moment, in: **Engineering mechanics : statics**, Prentice-Hall, Inc., New Jersey, 1999, pp. 179-180, 181, 182.